Experimental Observations of Damage States in Unnotched and Notched 3D Orthogonal Woven Coupons Loaded in Tension

Wade C. Jackson[1], Andrew C. Bergan[2], Nathaniel W. Gardner[3], and Cheryl A. Rose[4]

NASA Langley Research Center, Hampton, VA, 23681, U.S.A.

Kenneth N. Segal[5]

NASA Goddard Space Flight Center, Greenbelt, MD, 20771, U.S.A.

Nalinda W. Waas[6]

NIAR-ATLAS, Wichita State University, Wichita, KS, 67260, U.S.A.

This paper describes a series of unnotched and notched tensile tests on two 3D orthogonal woven architectures loaded in the warp direction. Dogbone specimens were used for the unnotched tests, and open-hole specimens were used for the notched tests. For each architecture and test type, two specimens were loaded under monotonic displacement control to failure, and two specimens were incrementally loaded to failure in five steps. X-ray computed tomography (CT) was used to characterize the woven architecture and defects on each specimen prior to testing. Digital image correlation (DIC) images were obtained from both sides of the specimen throughout the loading and unloading. For the incremental tests, X-ray CT was used to document the damage progression after each load increment. The results for both architectures and test specimens followed a similar pattern where matrix cracks formed perpendicular to the load direction and were primarily located between the stacks of warp tows. Two-piece failure path always occurred perpendicular to the loading direction, along the through-thickness segments of the Z-tows. The combination of stress concentrations due to the specimen geometry, weave geometry, and cut tows created stress concentrations that appear to initiate failure.

I. Introduction

Three-dimensional (3D) orthogonal woven composites offer reinforcement in all three directions. Some of the advantages of this class of materials include reduced notch sensitivity, near net-shape preforming, and improved through-thickness load carrying capability. The through-thickness reinforcement essentially eliminates delamination. Performance advantages may be gained in structures with complex shapes or with significant out-of-plane loads by using 3D woven composites. A more complete discussion of the current state-of-the-art in 3D orthogonal woven composites is available in recent review articles [1, 2]. In application of 3D orthogonal woven composites, the weave

---

[1] Senior Research Aerospace Engineer, Durability, Damage Tolerance, and Reliability Branch, MS 188E.
[2] Senior Research Aerospace Engineer, Durability, Damage Tolerance, and Reliability Branch, MS 188E, Senior Member.
[3] Research Aerospace Engineer, Structural Dynamics Branch, MS188E.
[4] Senior Research Aerospace Engineer, Durability, Damage Tolerance, and Reliability Branch, MS 188E.
[5] Aerospace Engineer, Mechanical Systems Analysis and Simulation Branch, Member.
[6] Research Engineer, Composites and Structures.

architecture is an additional design variable. As a result of the numerous permutations of weave architectures and loading conditions that arise, numerical simulation tools that can evaluate the performance of different architectures under relevant loading conditions are sought to reduce the empirical burden.

Numerous modeling approaches have been proposed for predicting the stiffness, strength, and damage tolerance of 3D woven materials, e.g., [2, 3, 4, 5, 6, 7, 8]. However, the maturity of these models remains low for several reasons that include the complexity of the tow architecture and associated difficulties with development of representative models, variations and defects that are unavoidable during the manufacturing process, and a lack of experimental understanding of the damage process during loading. Characterization of the damage and its progression is necessary to support the development of progressive damage analysis methods that can predict this damage behavior and therefore the strength and damage tolerance of 3D woven structures. Researchers have contributed by conducting test campaigns with post-mortem or incremental inspections. Warren et al. conducted quasi-static tension, compression, and in-plane shear tests on 3D orthogonal woven specimens fabricated with IM7 fibers and epoxy resin [9]. Post-mortem inspections showed debonding of the matrix from the tows was a common failure mechanism. Bogdanovich et al. used acoustic emission, digital image correlation (DIC), X-ray, and microscopy to determine damage initiation strain in the range of 0.4–0.6% [10]. Pankow et al. compared the response of orthogonal and layer-to-layer 3D woven S2 glass/SC-resin composite specimens loaded under quasi-static tension [11]. The DIC data revealed architecture dependent strain fields. Post-test visual inspection aided by dye penetrant showed matrix cracks developed following the tow boundaries and correlated spatially with the strain concentrations observed in the DIC data. Castaneda et al. also found good agreement between strain localizations observed in DIC and matrix cracks with locations and sizes correlated to the weave pattern [12]. Muñoz et al. reported the damage mechanisms in the warp and weft directions of 3D woven coupons with a hybridized architecture consisting of glass and carbon tows subjected to tensile loading [13]. The damage was imaged at various subcritical load levels with X-ray computed tomography (CT) and an X-ray opaque liquid to assist visualization. They found matrix cracking and tow debonding started at relatively low strains. These damage modes were arrested by fibers oriented across the crack plane and therefore had minimal effect on the stiffness.

This paper builds on the existing experimental body of work characterizing damage and its progression in 3D woven architectures by reporting the damage initiation and evolution behavior of 3D orthogonal woven carbon/epoxy coupons subjected to tensile loads. A series of unnotched and notched tensile tests were conducted on two different 3D orthogonal woven architectures. Understanding of the failure mechanisms was gained through the use of X-ray CT inspection and high-resolution DIC. The results of the experimental investigation provide an understanding of the complex failure mechanisms as well as a detailed record of damage development and progression throughout the loading history.

II.   Three-Dimensional Orthogonal Weave Architecture

Two 3D orthogonal weave architectures were selected for testing. The test specimens were woven with IM7 fiber tows and infused with RTM6 in a resin transfer molding process. The weaving was performed by Bally Ribbon Mills. The tests described herein were conducted on specimens from two panels, designated 3Z and 1Z. These two panels were woven with 6K tows and the weave patterns, as designed, are shown in Fig. 1. The primary difference between the two weave patterns is that panel 3Z has 13 layers of weft tows, 12 layers of warp tows, and three Z-tows per dent, whereas 1Z has 9 layers of weft tows, 8 layers of warp tows, and one Z-tow per dent. The design values for the unit cell dimensions and fiber content in the two weaves are summarized in Table 1. The panels were infused with resin and cured by North Coast Composites. The RTM-6 resin was first preheated at 80°C while the mold temperature was held between 120 and 140°C. The panels were then cured at 180°C for two hours.
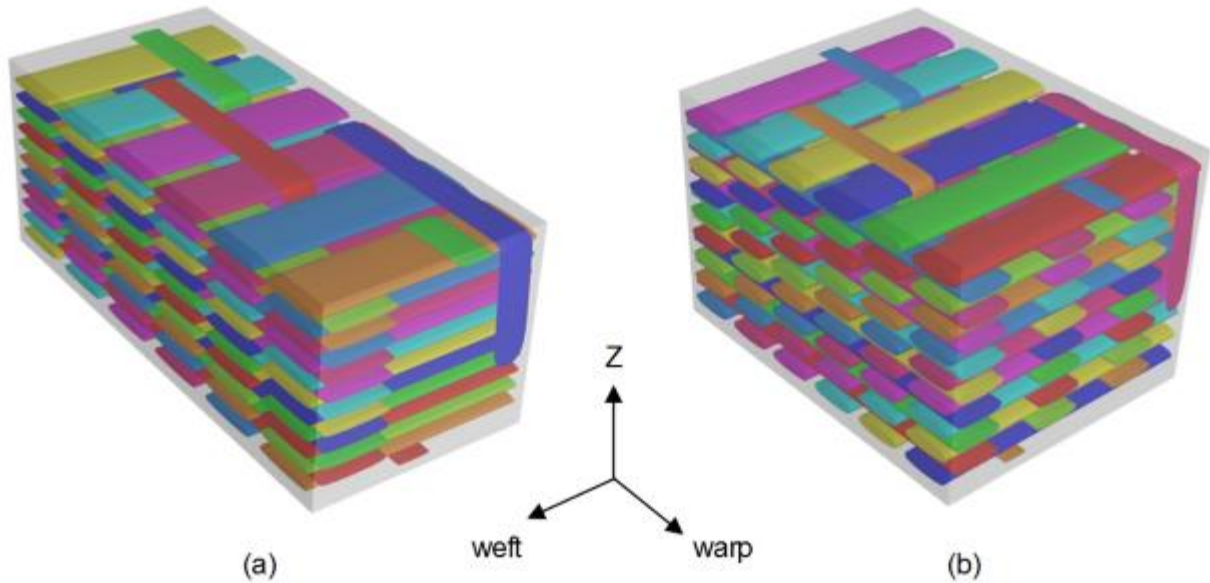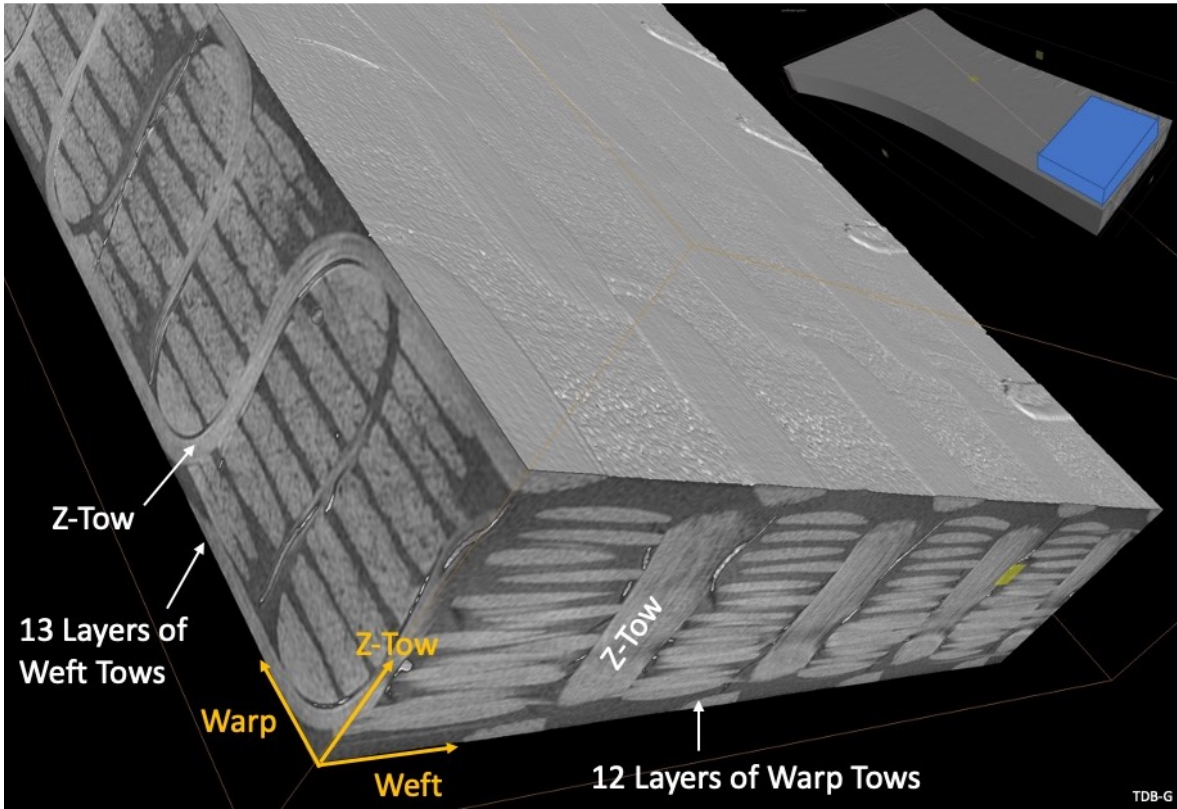
American Institute of Aeronautics and Astronautics

Fig. 1 Weave patterns used for the two panels (unit cells): (a) 3Z and (b) 1Z. The tow sizes and aspect ratios are arbitrary in this figure.
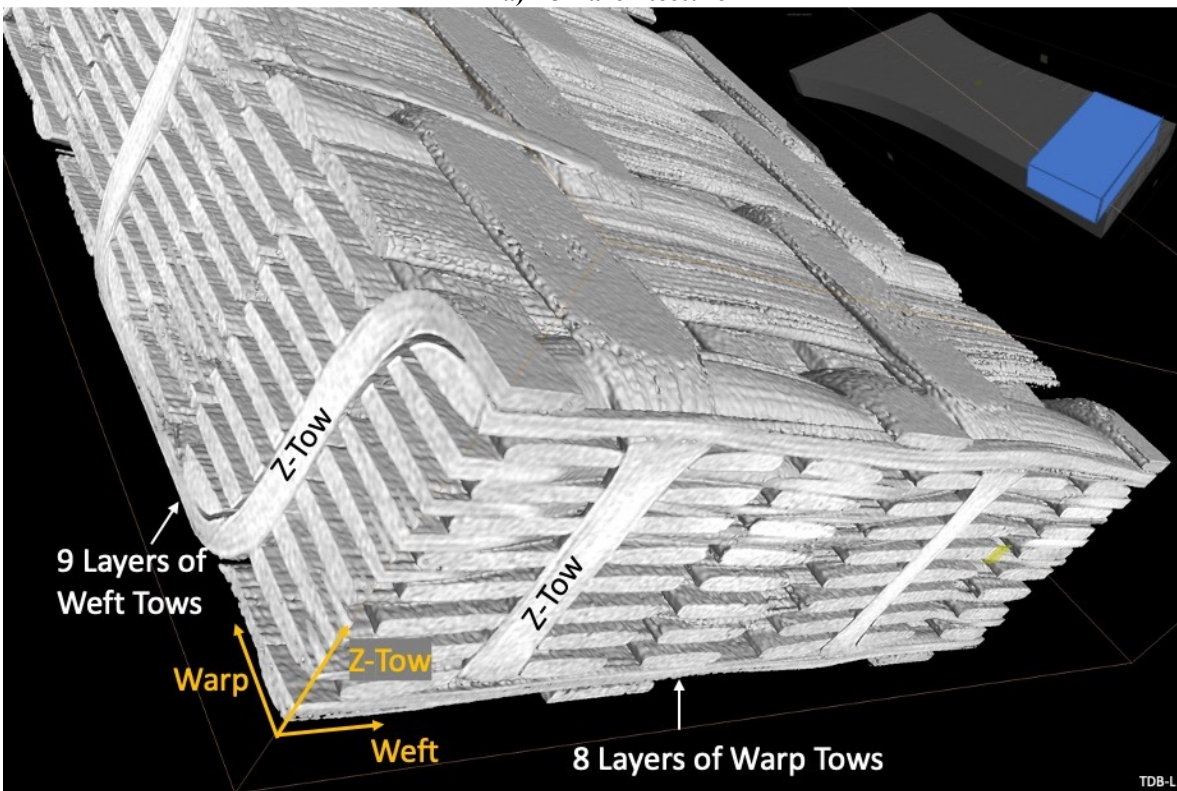
Table 1 Flat panel weave information.

Panel	Unit cell dimensions (inches)			Fiber content (%)			% fiber volume
	Warp	Weft	Z	Warp	Weft	Z	
3Z	0.378	0.125	0.125	28	60	12	54
1Z	0.324	0.189	0.125	40	51	9	50

Comparisons of the two weave patterns are shown in images from X-ray CT scans in Figs. 2 and 3 that were obtained prior to testing. Three-dimensional images are shown for architectures 3Z (Fig. 2a) and 1Z (Fig. 2b) where the images are cut to expose the Z-tow geometry. Note that the image of 1Z (Fig. 2b) shows the architecture with the resin hidden to better show the weave pattern. The obvious differences between the two architectures are the greater number of warp and weft layers in the 3Z architecture and the different pattern of the Z-tows. The Z-tows in both architectures pass over three weft tows on the surface before traversing the thickness again. In the 3Z architecture, however, multiple Z-tows are used between each warp tow such that a Z-tow penetrates the thickness between every weft tow instead of every third tow as in the 1Z weave. In-plane layers across the full width of the gage section of tension dogbone (TDB) specimens are shown for 3Z (Fig. 3a) and 1Z (Fig. 3b). The weft and warp layers shown are at or near the center thickness and have the through-thickness portion of the Z-tows highlighted in orange. The section at the top surface shows the loops of the Z-tows along with orange markings showing the paths connecting the Z-tow loops with the through-thickness Z-tow positions. Again, the greater number of Z-tows is obvious in the 3Z architecture where a Z-tow is located between every weft tow and between every warp tow to create continuous horizontal and vertical rows of Z-tows. For 1Z, a Z-tow penetrates the thickness after every third weft tow, and these penetrations are offset by one weft tow on adjacent warp tow gaps. Consequently, the Z-tows form a diagonal pattern compared to the orthogonal pattern in the 3Z architectures. Another point of interest relative to warp-direction tensile testing is that there are double the number of warp tows across the width for the 1Z weave compared to the 3Z weave. Conversely, the 3Z weave has 50% more layers of warps tows than the 1Z weave.

American Institute of Aeronautics and Astronautics

a) 3Z architecture

b) 1Z architecture (resin hidden)
Fig. 2 3D X-ray CT images showing fabric architecture of 3Z and 1Z panels.

American Institute of Aeronautics and Astronautics

a) 3Z architecture

Weft Layer   Warp Layer   Top Surface
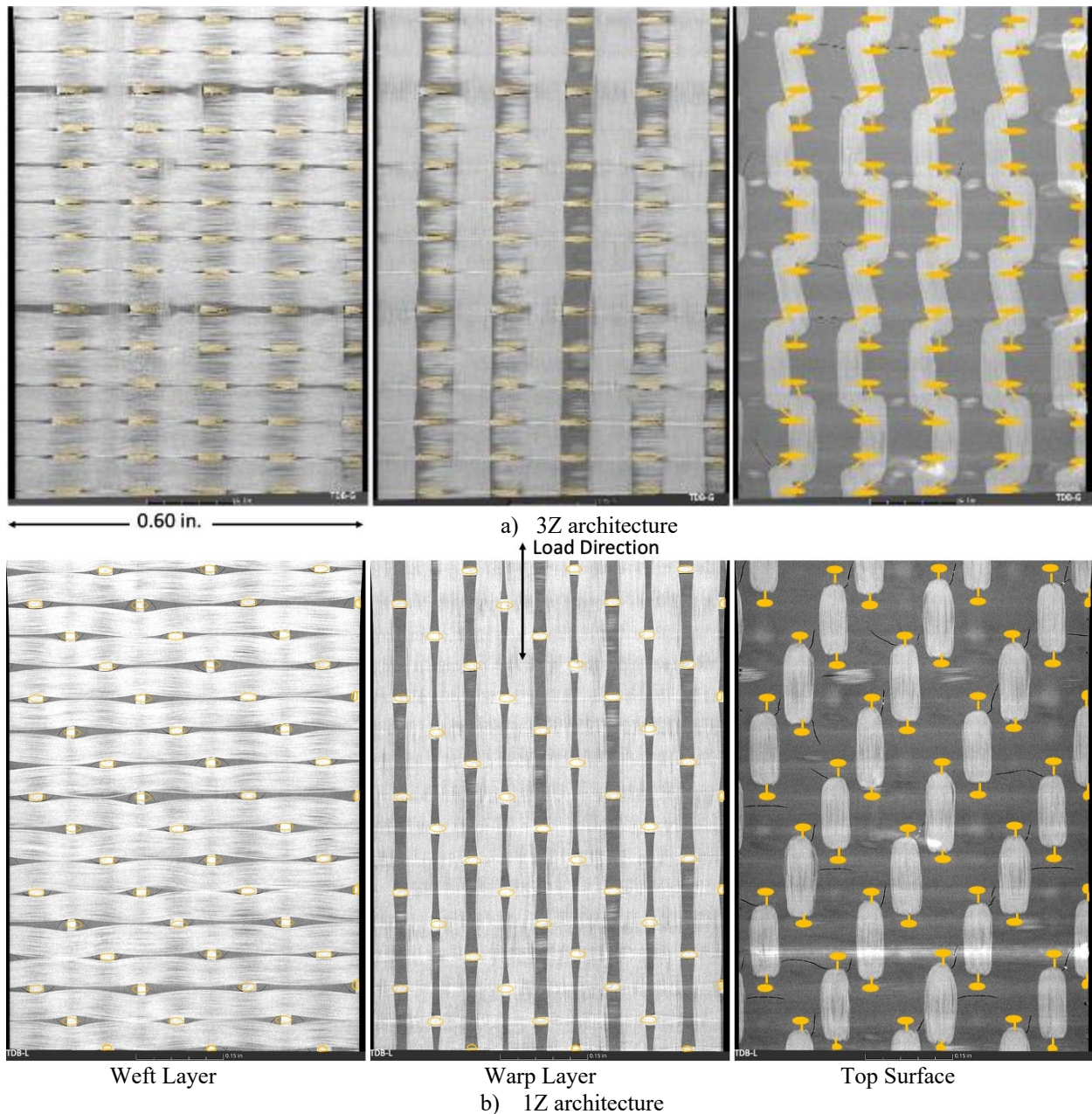
b) 1Z architecture

Fig. 3 X-Ray CT images across the TDB gage section through a layer of weft tows, a layer of warp tows, and a layer near the top surface for a) 3Z-TDB-G and b) 1Z-TDB-L specimens. The Z-tows are highlighted in orange in the interior layers. The orange markings on the surface show how the exterior loop connects to the through-thickness segment of the Z-tow.

III.   Test Specimens and Techniques

A dogbone specimen and an open-hole specimen were selected for the unnotched and notched configurations, respectively. Four TDB specimens were cut from each of the two panels with the length of the specimen aligned in the warp direction. These specimens were named, beginning with the panel number, 3Z-TDB-X (where X corresponds to the letters D through H) and 1Z-TDB-X (where X corresponds to the letters H though M). Similarly, four open-hole tension (OHT) specimens were cut from each panel with the length of the specimen also aligned in the warp direction. These specimens were named 3Z-OHT-X (X corresponds to T through W) and 1Z-OHT-X (X corresponds to D through G). The letter designation identifies the individual replicates. In the specimen images, label 218-09 refers to a panel with the 3Z weave, and label 219-10 refers to a panel with the 1Z weave. In addition to the specimen labels,

5

one of the four gripped surfaces of each specimen was labeled to ensure consistent alignment and orientation throughout the testing and scanning.

The dogbone specimens were 5.0-inches-long with a nominal width of 0.6 inches in the one-inch-long gage section as shown in Fig. 4. The average thickness of each specimen was obtained from several measurements spaced evenly along the length. The average thickness of each of the 1Z specimens ranged from 0.129 to 0.136 in., and the average thickness of each of the 3Z specimens ranged from 0.129 to 0.131 in. Similarly, the gage section widths averaged 0.599 to 0.601 in. for the 1Z specimens while the width averaged 0.600 in. all the 3Z specimens. The coordinate system shown in Fig. 4 includes both the material coordinate labels (uppercase) and test coordinate labels (lowercase). The test coordinate system (lowercase) was used in the DIC data reduction.
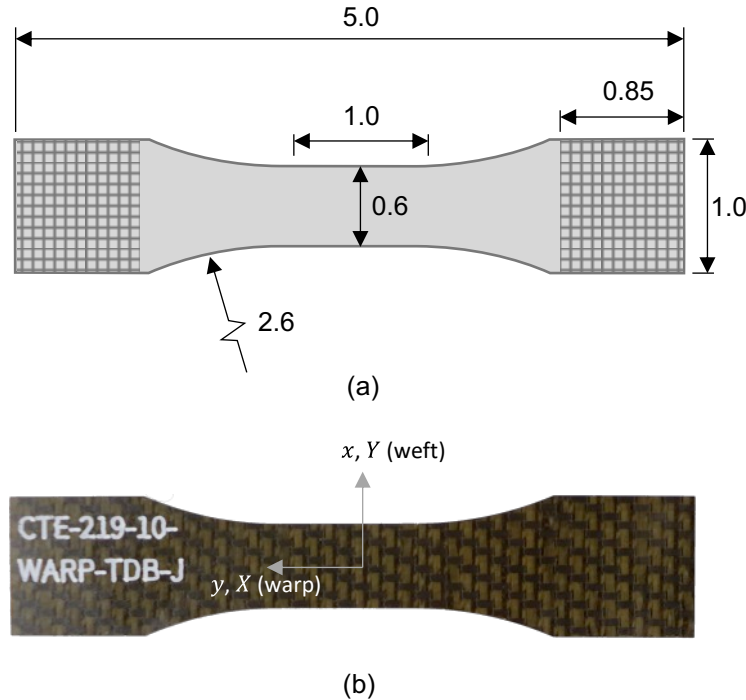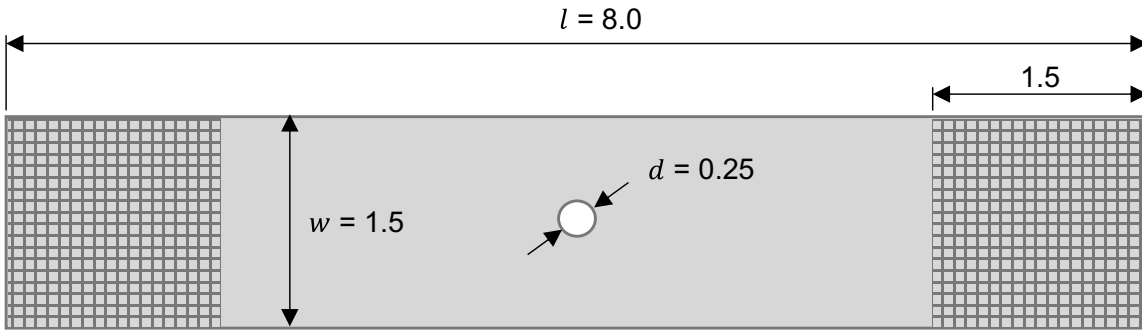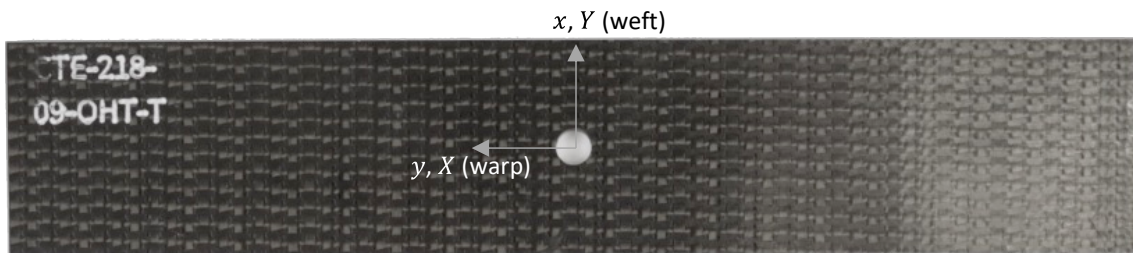

(a)

(b)

Fig. 4 Tension dogbone specimen configuration (a) schematic and (b) example photograph, showing the test (lowercase) and material (uppercase) coordinates (right-handedness should not be inferred). The crosshatch pattern in (a) indicates the gripped region. All dimensions are in inches.

OHT specimens with a 0.25-inch-diameter hole and 1.5-inch-width were fabricated in the configuration shown in Fig. 5 such that $w/d = 6$ and $l/d = 20$. The test specimens use the geometry recommended by ASTM D5766 [14]. Since the unit cell sizes and hole diameter were of the same order, some variability may be expected based on where the hole is located relative to the unit cell. Four specimens were fabricated from each flat panel, 3Z and 1Z, for a total of eight specimens. The specimens are designed X-OHT-Y where X is either 3Z or 1Z designating the panel and Y indicates the replicate (designated as a letter). The coordinate system shown in Fig. 5 includes both the material coordinate labels (uppercase) and test coordinate labels (lowercase). The test coordinate system (lowercase) is used in the DIC data reduction. The average thickness and average width for the 3Z specimens were 0.133 and 1.505 inches, respectively. For the 1Z specimens, the average thickness and average width were 0.128 and 1.506 inches, respectively. In all cases, the coefficients of variation of the thickness and width measurements were less than 0.5%. Since the letter designation for the specimen replicate is unique across the two panels for the results discussed, the panel label is not always listed.

American Institute of Aeronautics and Astronautics

(a)

(b)

Fig. 5 OHT specimen configuration (a) schematic and (b) example photograph, showing the test (lowercase) and material (uppercase) coordinates (right-handedness should not be inferred). The crosshatch pattern in (a) indicates the gripped region. All dimensions in inches.

All tests were performed under ambient conditions using a servo-hydraulic uniaxial load frame stand with hydraulic wedge grips. The test frame used a 22 kip load cell. Specimens were loaded in displacement control at a ramp rate of 0.01 inches/min. Test data/instrumentation included test stand cross-head displacement, force, displacement transducers attached to the specimens, high-resolution digital image correlation (DIC) systems on front and back surfaces, and real-time acoustic emission (AE). The OHT specimens also had four strain gages, front to back on either end near the grips. Fig. 6 shows an example of the test setup for an OHT specimen. Prior to testing, a high-resolution X-ray computed tomography (CT) scan was obtained on each specimen to document the woven architecture within the specimen and to identify defects (primarily cracks) from manufacturing and machining.

AE sensors were bonded onto all specimens and were monitored in real time during testing. The TDB specimens had one sensor at each end along the centerline and near the grips. The OHT specimens had two sensors at each end, which were spread out and placed near the specimen edges. The AE sensors were used as an aid to guide test interruptions (unloading points). The AE systems provided feedback that was useful for identifying damage initiation, progression, and times when large acoustic events occurred. The AE results are not discussed in this paper.

Two 3D 12 MP DIC systems were used to measure displacements on the front and back surfaces (normal to the z-direction). For the dogbone specimens, the region of interest included the constant-width cross section and the transition zone. On the side with the acoustic emission sensors, only a portion of the transition region could be captured. For the OHT specimens, the region of interest included the full width of the specimen and 2 in. of length centered on the hole. Image acquisition rate was 1 Hz for most of the test and was increased to 10 Hz near failure.

For each test series, two specimens were loaded monotonically to failure, and two specimens were loaded incrementally to failure. The tests were performed incrementally so that X-ray CT scans could be performed between test runs to investigate the damage formation and progression. Test interruptions on the incremental testing focused on damage initiation and damage formation near failure. Both real-time AE and real-time DIC were used to guide the test interruptions.
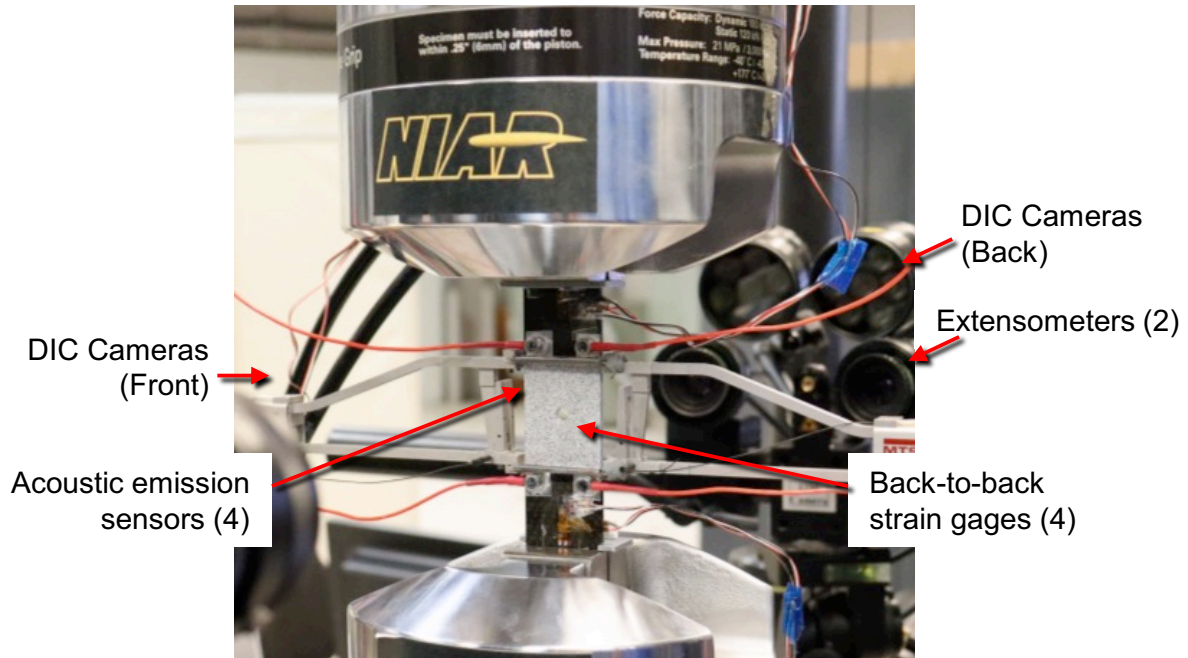
American Institute of Aeronautics and Astronautics

Fig. 6 OHT test configuration.

IV. Baseline X-Ray CT Inspection

All specimens were inspected by X-ray CT prior to testing to obtain a baseline condition. Since the TDB and OHT specimens were cut from the same panels, and all edges and holes were inspected and found to be free of damage as a result of the machining process, the general conditions were identical. Thus, only images from TDB specimens are shown in this section since they are representative of both types of specimens. In general, the baseline X-ray CT scans revealed significant cracking from the cure cycle. Typical defects are shown in an X-ray CT scan in Fig. 7 for the 3Z architecture. The majority of cracking was around, within, and branching from the Z-tows. Voids and splitting within the weft tows was also observed. The primary region of cracking was the resin-rich regions between the warp tow stacks. For the incremental test series, the initial cracks were noted and monitored for growth. Both the 3Z and 1Z specimens had very similar patterns of cracking, with the 1Z having more cracks connected to the surface. Cracks on the surface were readily identifiable in the X-ray CT and processed DIC data, and thus could be used to link X-ray CT observations of damage state evolution to particular load levels at which events were observed via DIC.
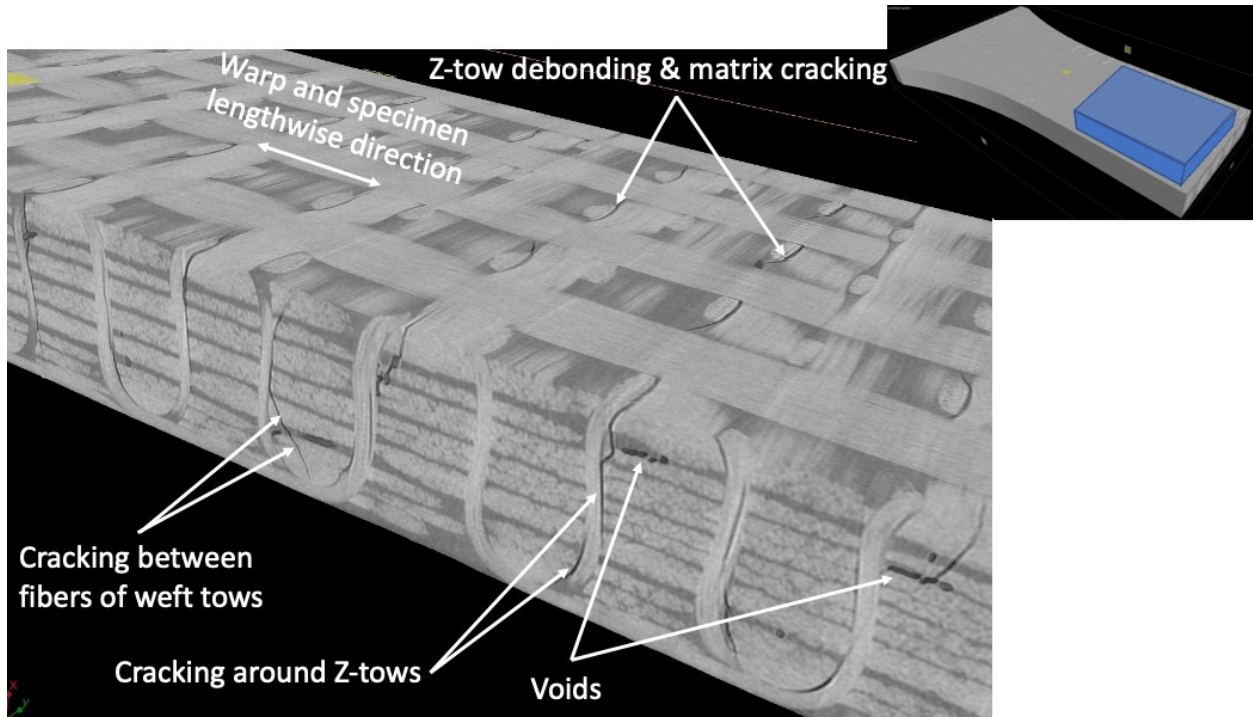
American Institute of Aeronautics and Astronautics

Fig. 7 Initial defects shown in a X-ray CT image of a 3Z dogbone specimen. Cut-planes on top and edges are shown to display interior damage.

Based on the typical morphological characteristics of cracks connected to the surface, three types of surface cracks were identified. The observations are summarized in a series of X-ray CT images shown in Fig. 8 for a 1Z TDB specimen consisting of the top surface and the adjacent weft layer (nearest to surface) in addition to three through-thickness sections. The first type of crack is associated with cracking around the Z-tows. Most of the Z-tows are debonded on one side, and this debonded region extends away from the Z-tows as a curved crack between the weft tows. This type of crack is shown in the top weft layer of Fig. 8 for most of the Z-tows (small ovals). An example is circled in yellow in the weft layer with the extension to the surface circled in yellow on the surface image of Fig. 8. In general, the orientations of these cracks at the surface vary and are not normal to the warp direction. Section A-A shows three cracks of this type connecting from the top surface (orange diagonal arrows) to the Z-tows (vertical tows). In the interior, these curved cracks around the Z-tows may extend to the resin-rich regions between the warp tows (see vertical orange arrows in section A-A in Fig. 8). The next two types of cracks are normal to the warp direction and located in the gap between two warp tow stacks. In the interior, these cracks have a small weft-direction dimension that corresponds to the distance between adjacent warp tows. Near the surface, these cracks extend in the width direction since they are no longer constrained by the warp tows and typically curve slightly on the ends. If the surface crack is above a weft tow stack that is adjacent to a Z-tow, the crack connects to the nearest Z-tow in the interior of the specimen in the gap between the warp tows (orange circles in Section C-C). In the other case where the crack is above the center stack of weft tows, the crack will extend through the thickness in the gap between the warp tows and will stop when it contacts the interior surface of the Z-tow on the opposite surface of the specimen (green circle in Section B-B).
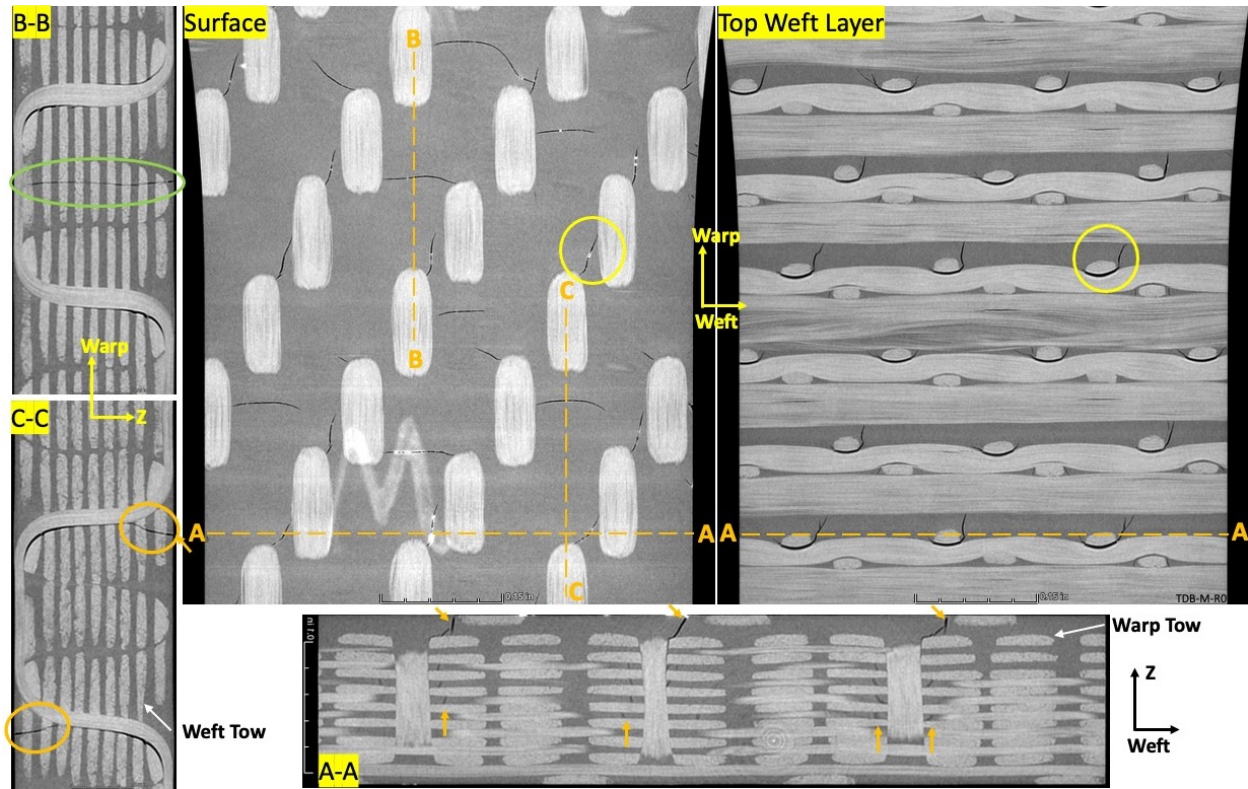
American Institute of Aeronautics and Astronautics

Fig. 8 X-ray CT images tracing surface cracks for the 1Z architecture.

Pre-test X-ray CT images are shown in Fig. 9 for a TDB specimen with the 3Z architecture. Few surface cracks were present on the specimen prior to testing as shown on the surface image in Fig. 9. The weft layer just below the surface shows cracking around many of the Z-tows similar to the cracking observed in the 1Z architecture (cracks highlighted in orange). Most of the cracks on the surface are connected to these internal Z-tow cracks. One crack on this image (orange circles on the planar images and Section A-A) was identical to the type found in the 1Z architecture. In this type of crack, a weft-direction surface crack located between warp tows joins with an internal Z-tow. The crack splits the fibers in several weft tows as it connects between the surface and the through-thickness portion of the Z-tow. One possible explanation for the reduced amount of surface cracking compared to the 1Z architecture is that the gaps between the warp tows are mostly covered on the surface by the Z-tow loops. Other weft direction surface cracks (yellow circles in Section B-B) are located only near the surface and stop at the first warp tow layer.
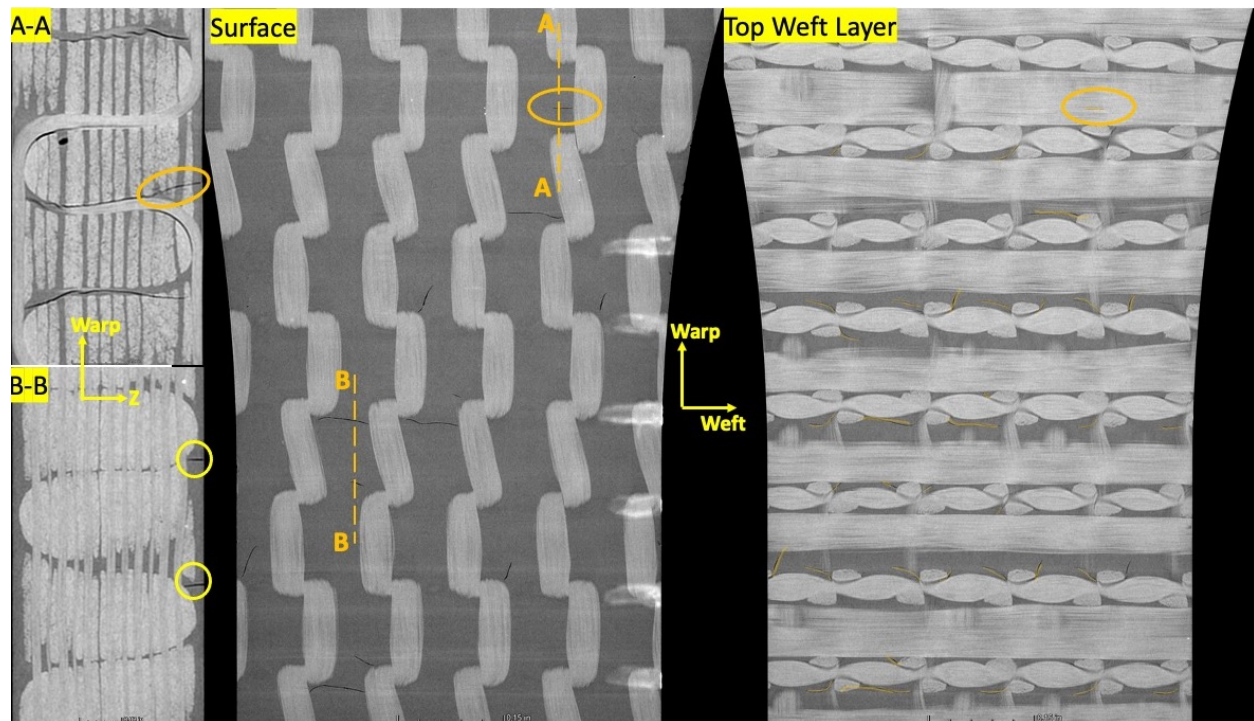
American Institute of Aeronautics and Astronautics

Fig. 9 X-ray CT images tracing surface cracks for the 3Z architecture.

V. Tension Dogbone (TDB) Results

For each panel architecture, two specimens were loaded to failure followed by incremental testing of two specimens. For the TDB tests, the average failure loads were 6411 lbs. (CV= 5.7%) and 7947 lbs. (CV=3.4%) for specimens from panels 3Z and 1Z, respectively. The following sections discuss the overall structural response, the failure response, development of surface cracking during loading, and then the progressive damage.

A. Structural Response

The overall structural response of the TDB specimens was very linear up to an instantaneous failure event, where the load dropped to near zero. The stress vs. strain responses of the eight test specimens are shown in Fig. 10. Specimens E to H are from panel 3Z, and specimens J to M are from panel 1Z. Stopping points for the incrementally loaded specimens are marked with symbols. The data are from one of the two DIC systems. The DIC-measured displacement data is preferred over the crosshead displacement since it allows for measurement of displacement over the constant cross-section region and omission of effects due to the transition region and gripping. The stress is computed from the load as recorded by the DIC system divided by the original cross-sectional area in the gage section. The axial (warp) strain is computed from DIC results using a virtual extensometer with a 1-inch gage length centered on the coupon (as shown in the inset on the right of the figure). The displacements at the two points used in the virtual extensometer were each an average over a 0.001 in^2 square area to reduce noise. However, some variability in this measurement may occur due to the location of the averaging area relative to the unit cell. The initial stiffness is obtained from this stress-strain data via a linear fit over the range 0.05% to 0.20% strain. The average stiffness of each weave is shown with the black dashed lines in Fig. 10. These average stiffnesses are also reported in Table 2, showing very good repeatability among the four tests for each panel. At high strains, for panel 1Z, the four specimens show a small reduction in stiffness, whereas for panel 3Z, three of the four specimens show a small increase in stiffness. The nominal strengths and strain-to-failure are also reported in Table 2. The strengths are nominal since failures did occur within the gage section.
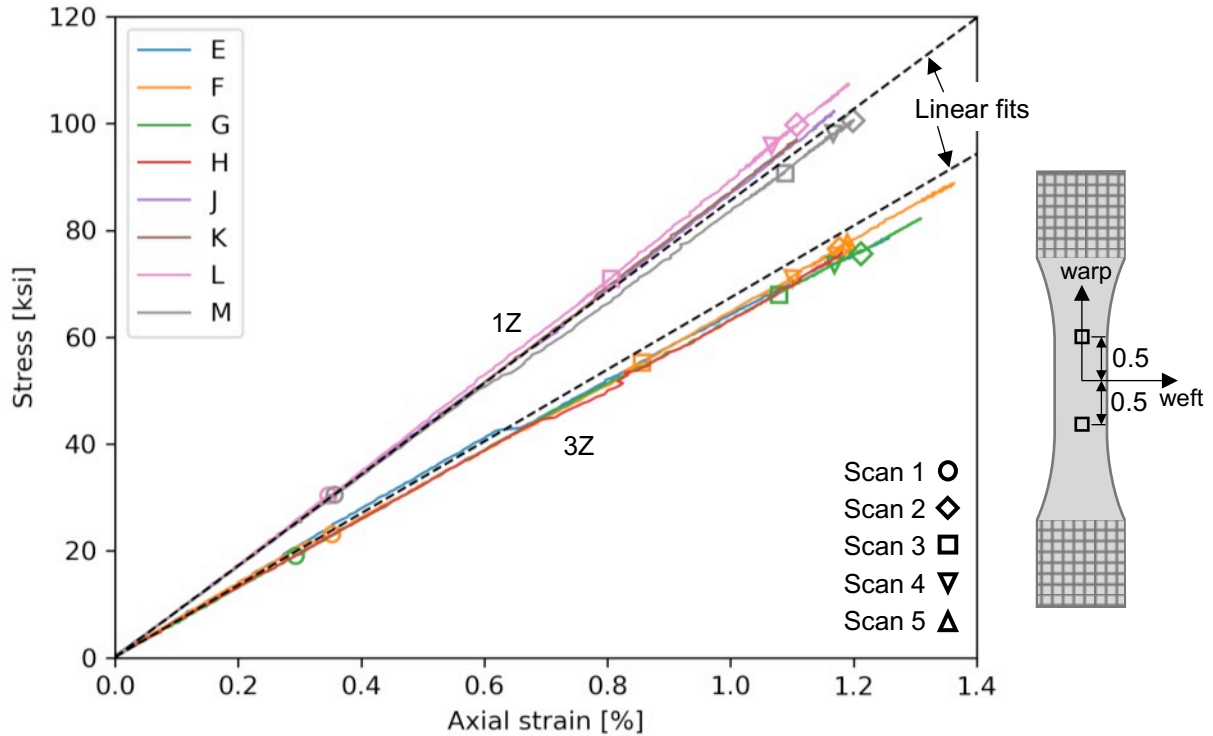
American Institute of Aeronautics and Astronautics

Fig. 10 Axial stress vs. strain response for the eight TDB specimens from DIC measurement over a 1-inch gage length. Dimensions are in inches.

Table 2 TDB stiffness and strength for the two weaves (panels).

Panel	Stiffness		Nominal Strength		Strain-to-failure	
	Avg. [ksi]	CoV [%]	Avg. [ksi]	CoV [%]	Avg. [%]	CoV [%]
3Z	6731	2.7	81.0	6.7	1.28	5.3
1Z	8550	1.3	101.7	4.2	1.17	3.1

B. Failure Response

All TDB specimens failed abruptly without any significant indications of imminent failure. Photographs of all failed specimens are shown in Fig. 11. Fractures were located at or near where the curved edges transition into the straight section and were straight across the width. Visual inspection clearly shows fiber fracture of the load bearing warp tows. Some secondary damage, marked with red arrows, did occur away from the primary fracture due to the dynamic release of energy at failure.

American Institute of Aeronautics and Astronautics
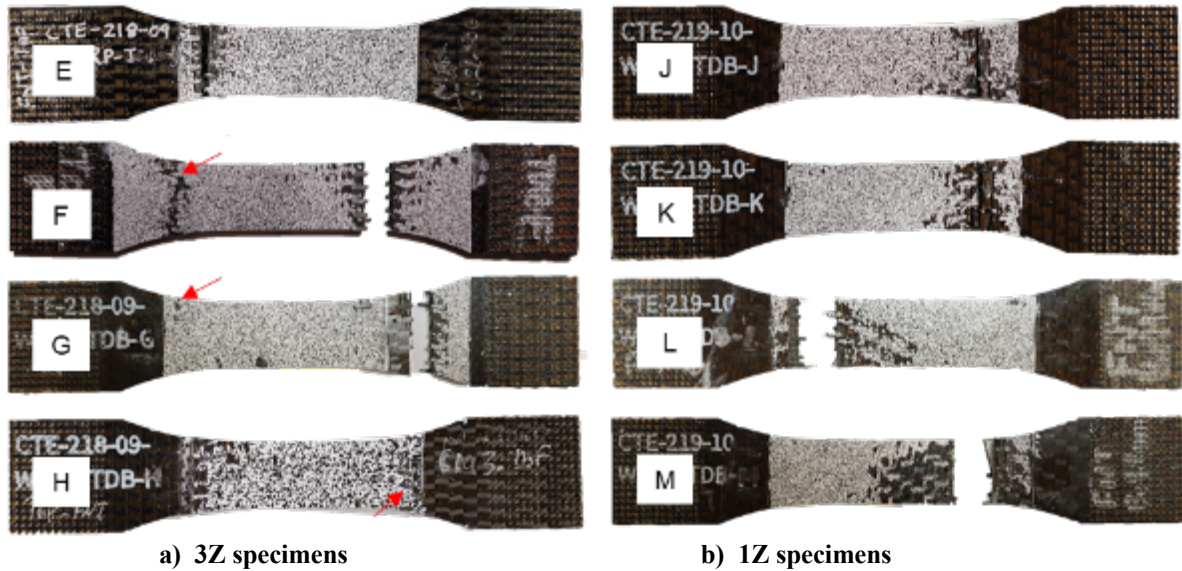
a) 3Z specimens   b) 1Z specimens

Fig. 11 Post-failure photographs of the eight TDB specimens. Red arrows mark secondary damage that likely occurred as a result of the stress wave after the primary failure.

Several specimens of each architecture were inspected using X-ray CT following failure. The fractures of specimens TDB-H and TDB-G are shown in Fig. 12 for sections near the mid-thickness. Tensile failures in laminated composite test coupons are typically difficult to inspect due to extensive delamination near the fracture. However, the Z-tows in the woven specimens limited secondary delaminations. Hence inspection of the fracture surfaces was straightforward. Specimen TDB-H failed near the upper transition region while TDB-G failed near the lower transition region. Both specimens show straight fractures across a horizontal row of Z-tows (circled). The fracture paths coincide with the intersection of a row of Z-tows and the termination of a warp tow along the transition region. The ends of the warp tows in the transition region are marked with yellow arrows. The combination of stress concentrations from the warp tows ending and the Z-tows near the edge produce a likely failure initiation site. This stress combination is probably the reason that all TDB specimens failed in the transition zone near the straight gage section. On specimen TDB-H (Fig. 12a), warp tows on both sides of the specimen terminate at the fracture. On specimen TDB-G (Fig. 12b), only the left side of the fracture intersects with the end of a warp tow. On the right side, the warp tow terminated closer to the straight gage section and produced a crack that fractured the stack of warp tows nearest to the edge. Thus, apparently this potential failure location competed with the final failure location.
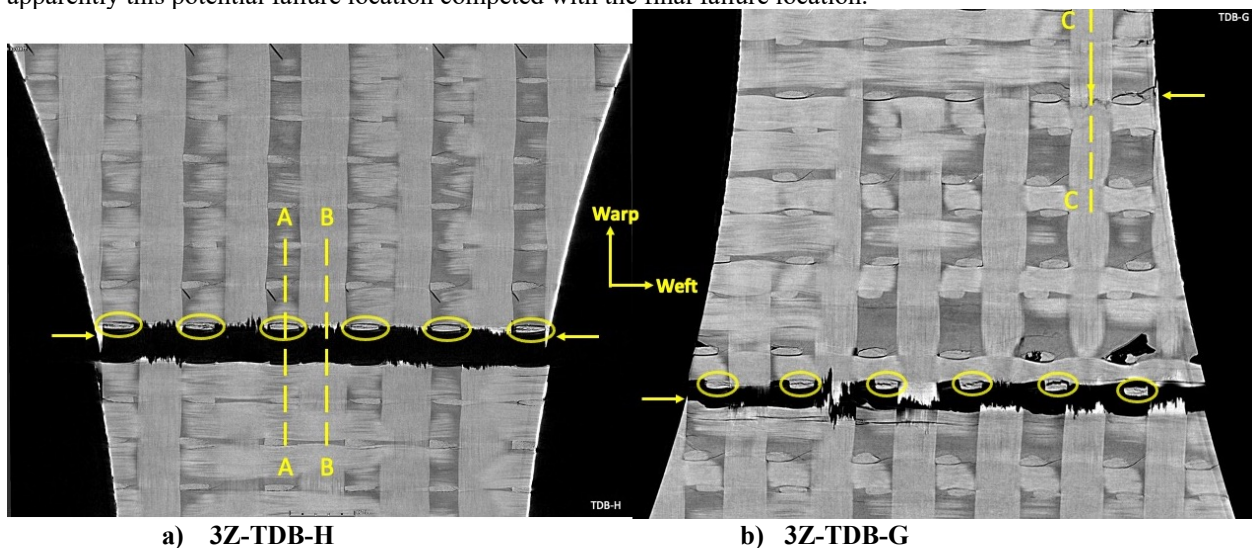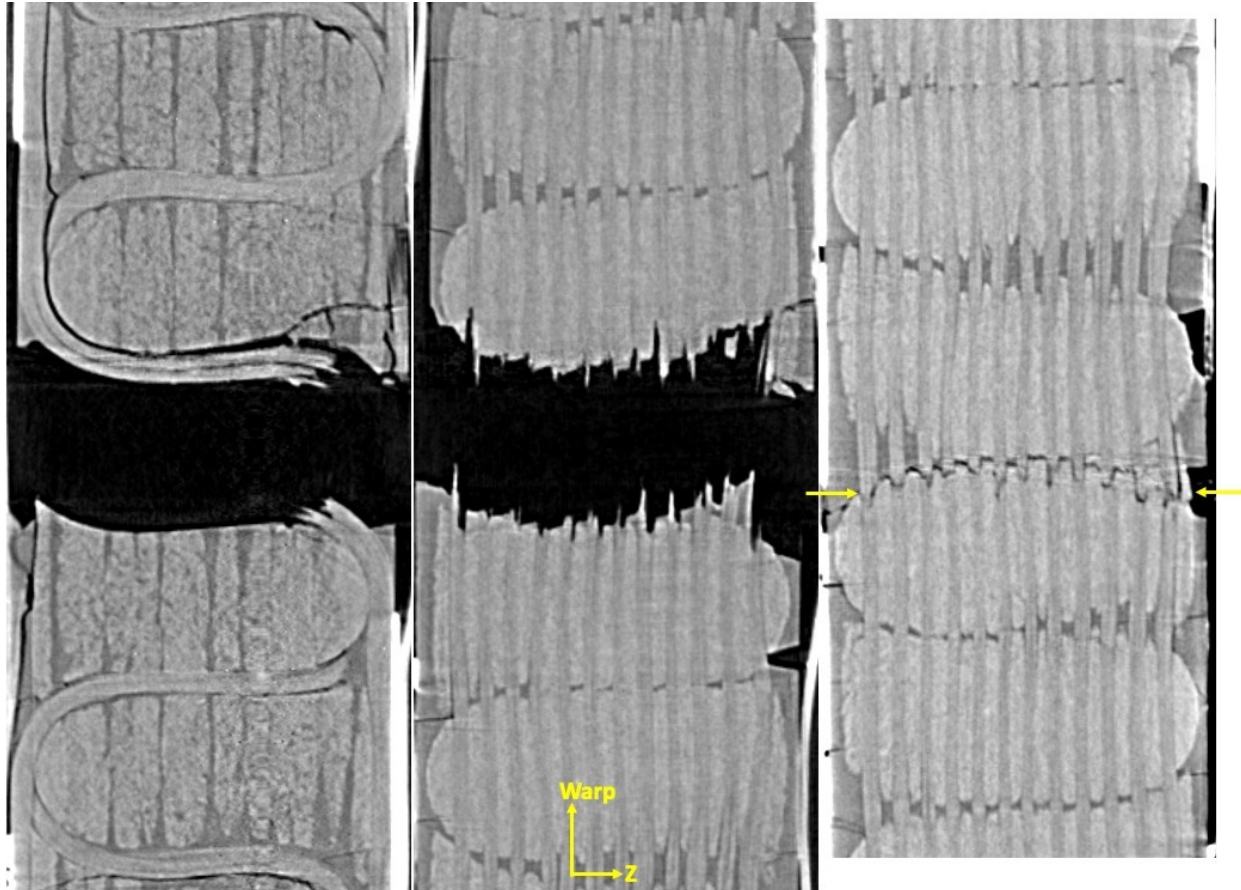

a) 3Z-TDB-H   b) 3Z-TDB-G

Fig. 12 X-Ray CT images showing interior fractured warp tows across the width of specimen a) 3Z-TDB-H and b) 3Z-TDB-G. Warp-direction cross sections are shown in Fig. 13.

13

American Institute of Aeronautics and Astronautics

Through-thickness cross sections along the warp direction corresponding to the dashed lines in Fig. 12 are shown in Fig. 13. For specimen TDB-H, Sections A-A and B-B show the Z-tow fracture near where it turns through-the-thickness and the adjacent warp tow fractures, respectively. The warp tow fracture follows the gap between the stacks of weft tows which also matches the adjacent Z-tow path. In section C-C, the horizontal arrows point to an additional warp tow fracture zone located at the end of the terminated warp tows but away from the primary fracture.
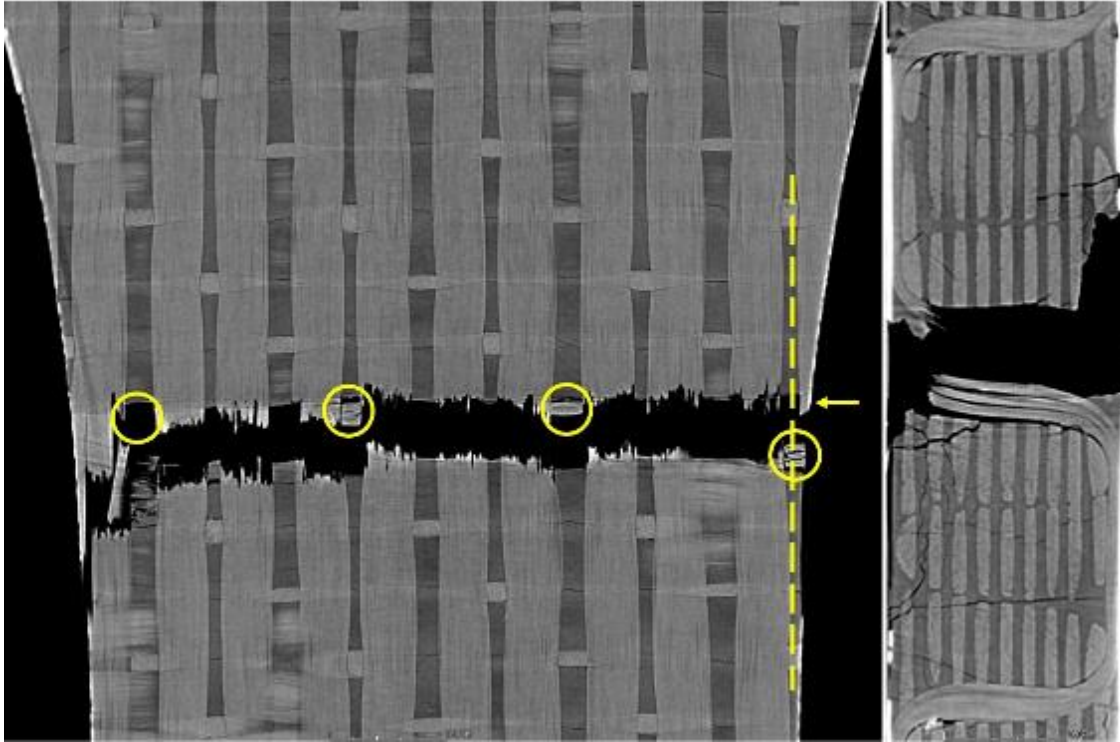

a) TDB-H Section A-A   b) TDB-H Section B-B   c) TDB-G Section C-C

Fig. 13 X-Ray CT sections showing fractures along the warp direction for 3Z specimens TDB-G & H. Arrows in Section C-C indicate a stack of fractured warp tows away from primary failure.
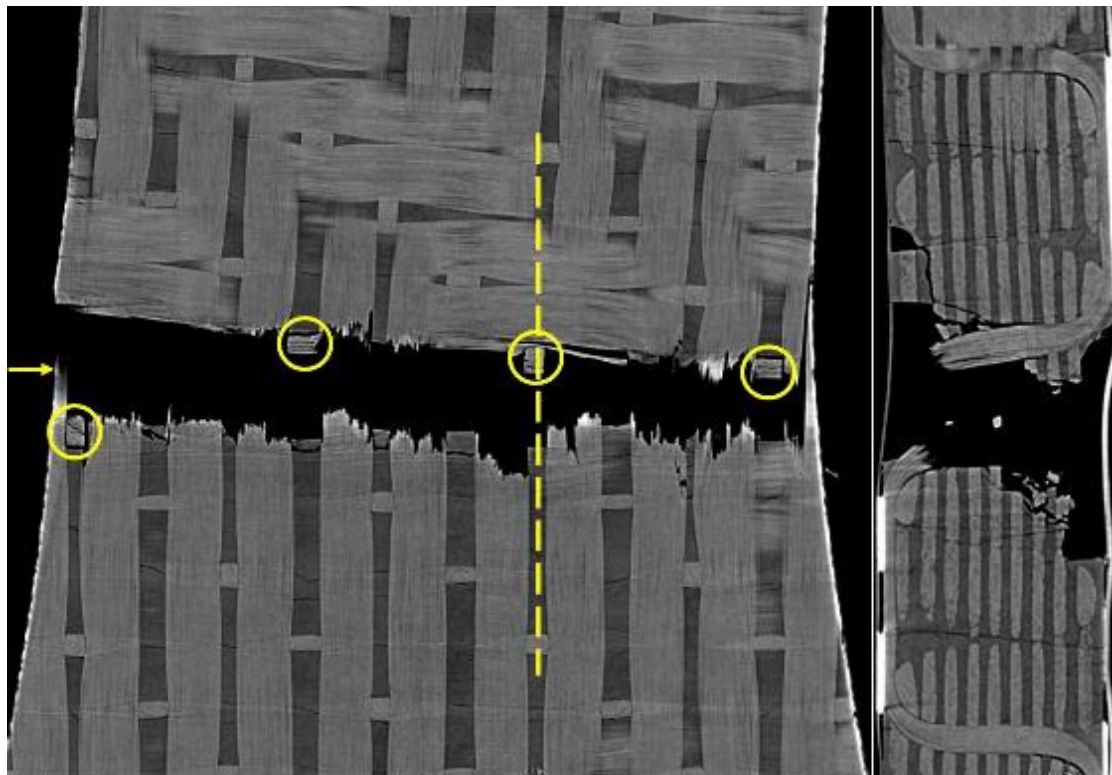
X-ray CT images of failed specimens from panel 1Z are shown in Figs. 14 and 15. Similar to specimens from panel 3Z, the fractures pass through a horizontal row of Z-tows (circled). However, the fracture path is more ragged and does not appear as straight since each Z-tow along the fracture path is separated by three warp tows instead of one. As marked with arrows, each fracture path can be traced back to a terminated warp tow near an edge Z-tow. Sections between the warp tows show the fracture occurring at the Z-tow, with similar characteristics to the 3Z specimens.

American Institute of Aeronautics and Astronautics

a) Slice showing warp tow fracture near mid-thickness   b) Slice from Fig. 14a line

Fig. 14   X-ray CT images showing failure in specimen 1Z-TDB-L. The arrow marks the edge termination of a warp tow. The circles mark the location of the z-tows along the failure surface.

a) Slice showing warp tow fracture near mid-thickness   b) Slice from Fig. 15a line

Fig. 15   X-ray CT images showing failure in specimen 1Z-TDB-M. The arrow marks the edge termination of a warp tow. The circles mark the location of the z-tows along the failure surface.

American Institute of Aeronautics and Astronautics

C. Surface Cracking

Surface cracking is one of the easier damage characteristics to track and was the first indication of damage formation observed while running the tests. Surface cracks were observed prior to testing and new cracks were detected at relatively low load levels (20-30% of failure load) for all specimens. The DIC systems were used to highlight the initiation and growth of these cracks using the uncertainty coefficient sigma [15]. Sigma correlates well with cracking since the associated displacement jump across the crack reduces the certainty of correlation. Sigma is plotted with a range of 0 to 0.015 pixel, which was found via manual inspection to show cracks with the highest values (red-most) colors on the colorbar. Contour plots of sigma at five load levels from TDB specimens E (3Z) and K (1Z) are shown in Fig. 16. The accumulation of cracks (red regions) occurs through the load history starting between 20 and 40% of peak load and reaching saturation around 90% of peak load.

(a) Specimen E

(b) Specimen K

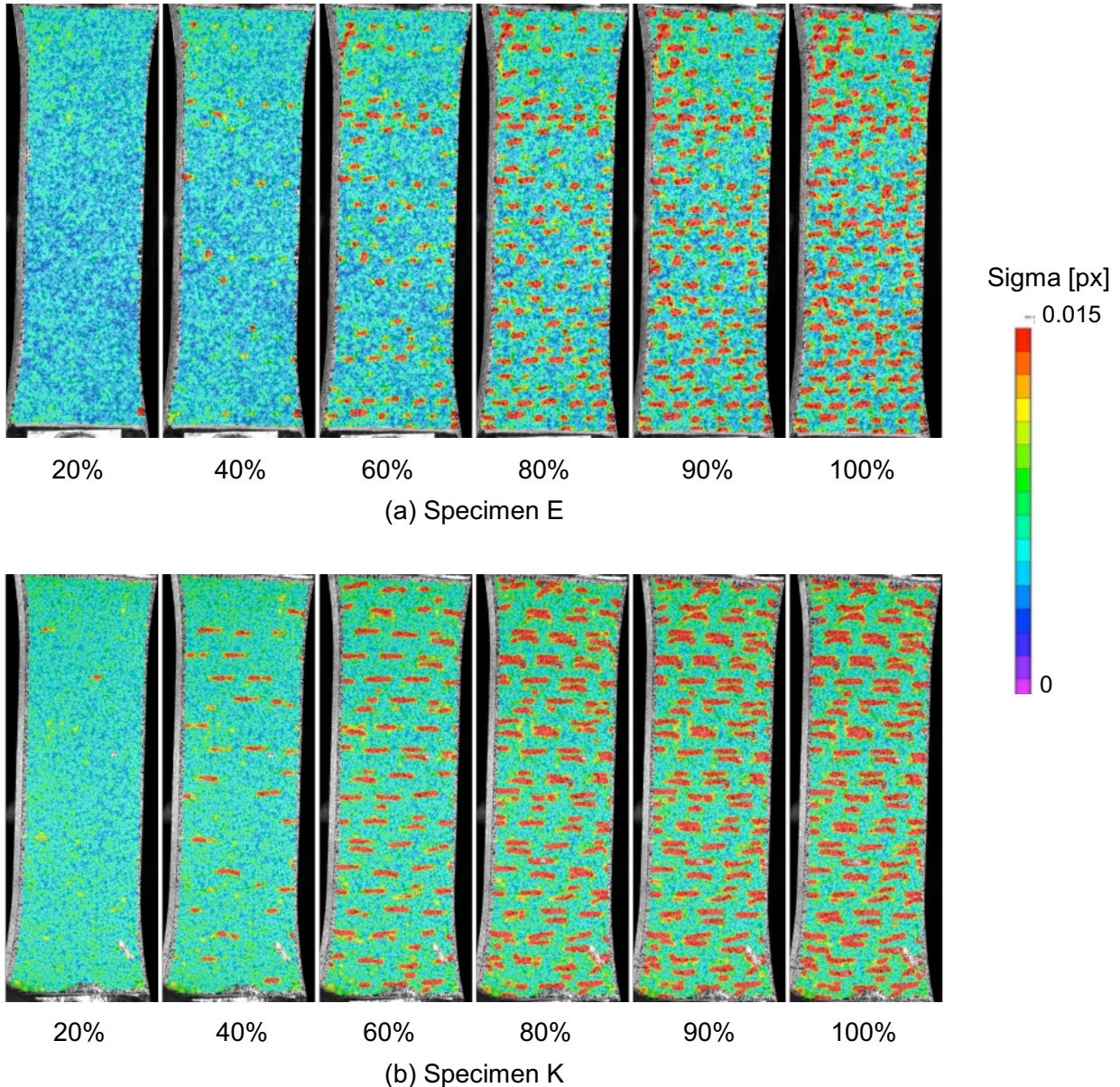**Fig. 16 DIC uncertainty coefficient contour plots for two TDB specimens, with color scale selected to highlight surface cracking.**

Since surface cracks were very evident in the DIC data, the data was processed to count the number of surface cracks at each image pair. Automatic identification and counting of cracks was possible via identifying and counting

16

American Institute of Aeronautics and Astronautics

the number of red blobs in the image. A crack counting algorithm was developed using L*a*b* color space color-based segmentation in Matlab [16]. The procedure gives an approximate number of cracks, judged based on manual inspections to have an error band of about ±10%. Errors were caused by overlapping red sigma blobs and missing DIC data. The crack counting algorithm was applied to the constant-width gage section in the TDB specimens (Fig. 17). Surface cracks start to accumulate between 0.2% and 0.4% axial strain. Subsequently, a linear increase in the number of cracks with similar slope was observed in the four specimens. A plateau of around 60 cracks was reached at about 0.7% axial strain in the 3Z specimens (E, H). A plateau with a similar number of cracks was also reached for the 1Z specimens (J, K) but at a higher strain, around 1%.
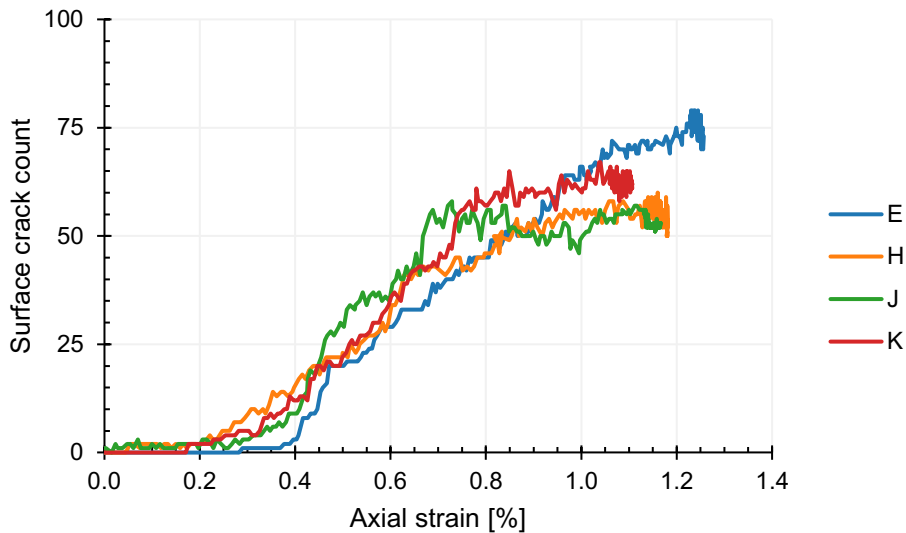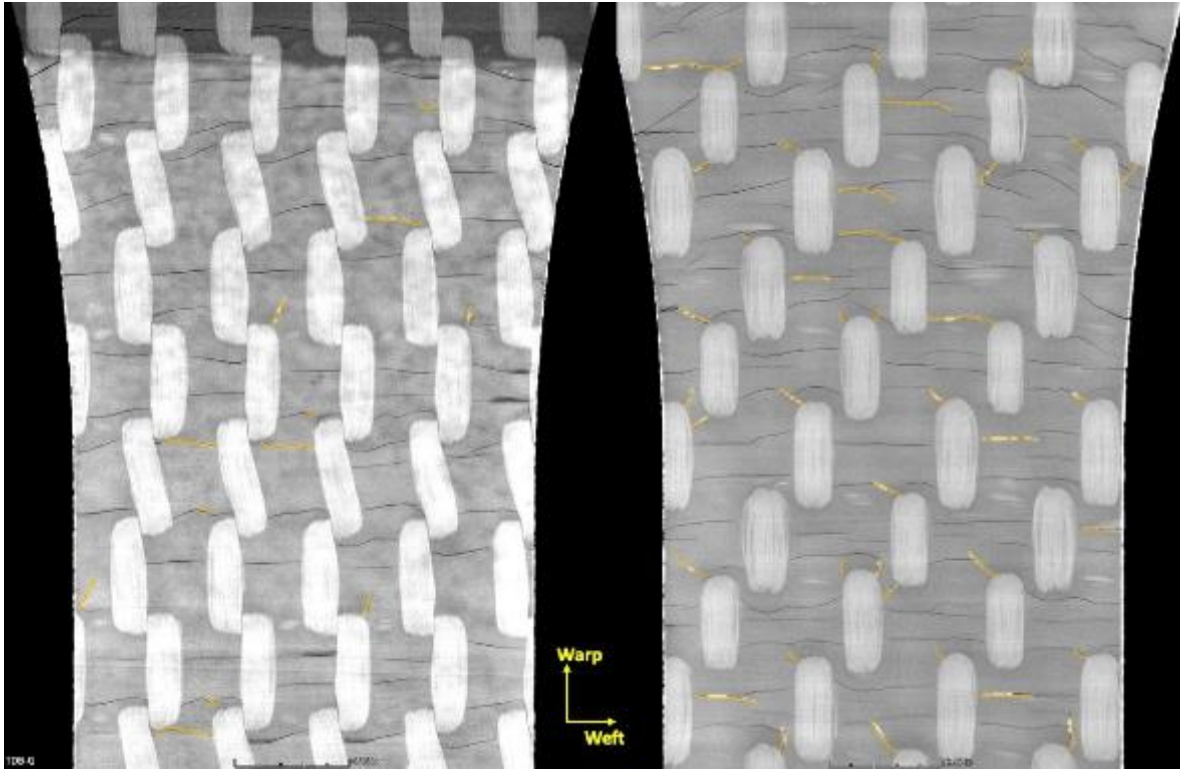

Fig. 17 Results of crack counting algorithm showing surface crack accumulation through the load history.

The surface cracks are also easily observed in the X-ray CT images. Images, just prior to failure, of the surface cracks are shown in Figs. 18a and 18b for two intermittently loaded specimens 3Z-TDB-G and 1Z-TDB-M, respectively. The cracks that were present from manufacturing are highlighted in orange. Both woven architectures show extensive surface cracking, with the 1Z having more cracks. New surface cracks generally formed transverse to the load (crack surface normal to the warp direction). Details relating these exterior cracks to interior damage are presented in the following section.

17

American Institute of Aeronautics and Astronautics

a) 3Z-TDB-G at 93% of failure load   b) 1Z-TDB-M at 100% of failure load
Fig. 18 Surface cracking shown in X-ray CT images. Manufacturing cracks are highlighted in orange.

D. Internal Damage

The specimens that were subjected to interrupted loading and X-ray CT scanning have the stopping points marked with symbols in Fig. 10. In general, the approach in choosing the stopping points was for the first stop to capture the damage state at the first indications of damage and then to attempt to capture the damage state as close as possible to the max load with the subsequent stops. The interrupted loading run load levels are summarized in Table 3. After the last interrupted loading, the specimens were loaded to failure to obtain a strength, F_{max}. In the case of specimen M, the final loading (run 5) did not achieve a higher load than the previous loading (run 4). This behavior can be attributed to viscoelastic effects in the material.

American Institute of Aeronautics and Astronautics

Table 3 TDB interrupted test load levels.

Panel	Specimen	Run	Fraction of strength [%]	Fraction of average strength [%]
3Z	F	1	26.2	28.7
		2	62.3	68.1
		3	80.0	87.5
		4	86.1	92.4
		5	87.6	95.8
		6	100.0	109.4
	G	1	23.3	23.6
		2	82.9	84.2
		3	89.4	90.8
		4	92.6	94.0
		5	100.0	101.5
1Z	L	1	28.3	29.9
		2	66.1	69.8
		3	89.1	94.0
		4	92.8	97.9
		5	100.0	105.6
	M	1	30.3	29.9
		2	90.2	89.0
		3	97.4	96.1
		4	100.0	98.6
		5	99.5	98.1

For the incremental tests, initial and post-incremental X-ray CT scans were conducted to track damage as a function of load history. In Fig. 19 (3Z-TDB-G) and Fig. 20 (1Z-TDB-M), representative through-thickness slices were extracted at identical locations on each specimen to examine the damage states between runs. Since damage formed primarily in the gap between the warp tows, only these sections are shown. For the initial damage state shown in the slice for 3Z-TDB-G (Fig. 19a), the primary defects are Z-tow debonding (green arrows) and cracks splitting off from the Z-tows and branching towards the surface (orange circles). These cracks are identical to surface cracks discussed earlier but have not connected to the surface. For the slice after 28% of F_{max} (Fig. 19b), two more similar cracks have developed from the Z-tows (yellow circles) which connect to the surface to form a surface crack. After 83% of F_{max} (Fig. 19c), new cracks (yellow circles) are observed branching from the Z-tows with some connecting to the surface. In addition, existing cracks have extended, such as the initial crack shown in Fig. 19a, which now connects with the surface to form a new surface crack (red circle). Hence, in the 3Z specimens, the observed matrix cracks due to loading have similar characteristics to the matrix cracks resulting from the cure process. No new damage initiation or growth was observed in the X-ray CT slices after loading to 89% and 93% of F_{max}.

American Institute of Aeronautics and Astronautics

a) Initial   **b) 28% of failure load**   **c) 83% of failure load**
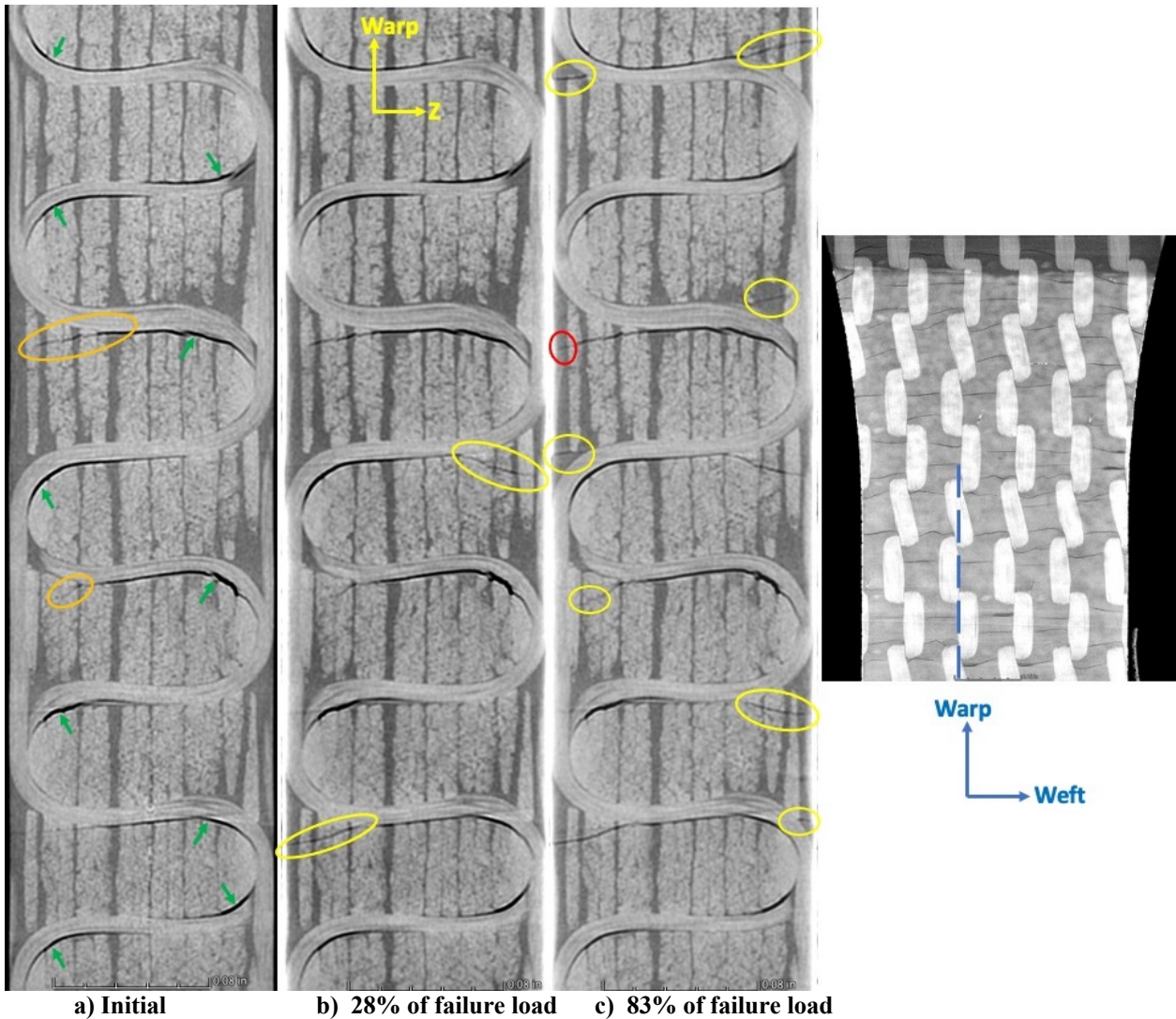
Fig. 19   Interior cracking 3Z-TDB-G shown in X-ray CT slices between the warp tows. Surface image shows the slice location. Orange circles indicate initial damage. Green arrows indicate initial Z-tow debonding. Yellow circles indicate new damage development.

Fig. 20 shows a similar sequence of X-ray CT images for the 1Z architecture for specimen TDB-M. In the initial pre-test section (Fig. 20a), two cracks are shown connecting Z-tows to surface cracks (circled). Debonded Z-tows are indicated by the green arrows. In the second cross section after the specimen was loaded to 30% of failure load, two new cracks are shown (circled). The upper crack (yellow circle) is similar to the initial cracks and those found in the previous figure for the 3Z-TDB-G specimen. A new type of interior crack formed that splits two stacks of adjacent weft tows but does not connect to the surface or a Z-tow (purple circled crack). On the last section taken after a ramp to 93% of F_{max} (Fig. 20c), cracks formed between every stack of adjacent weft tows (purple boxed cracks). These cracks have morphology similar to the one identified in the previous loading, but some connect to the surface. The interior crack from the previous ramp extended to the surface to form a new surface crack (red circle). In addition to the cracks between the stacks of weft tows, new through thickness cracks developed within stacks of weft tows (purple boxed cracks). These cracks within the weft tow stacks terminated on one side at or near the surface Z-tow and at or near the surface on the other side. Thus, in the 1Z specimens, matrix cracks develop under load near the Z-tows following a similar morphology to the cure-induced cracking; and at high loads, additional cracks develop between and within stacks of weft tows.

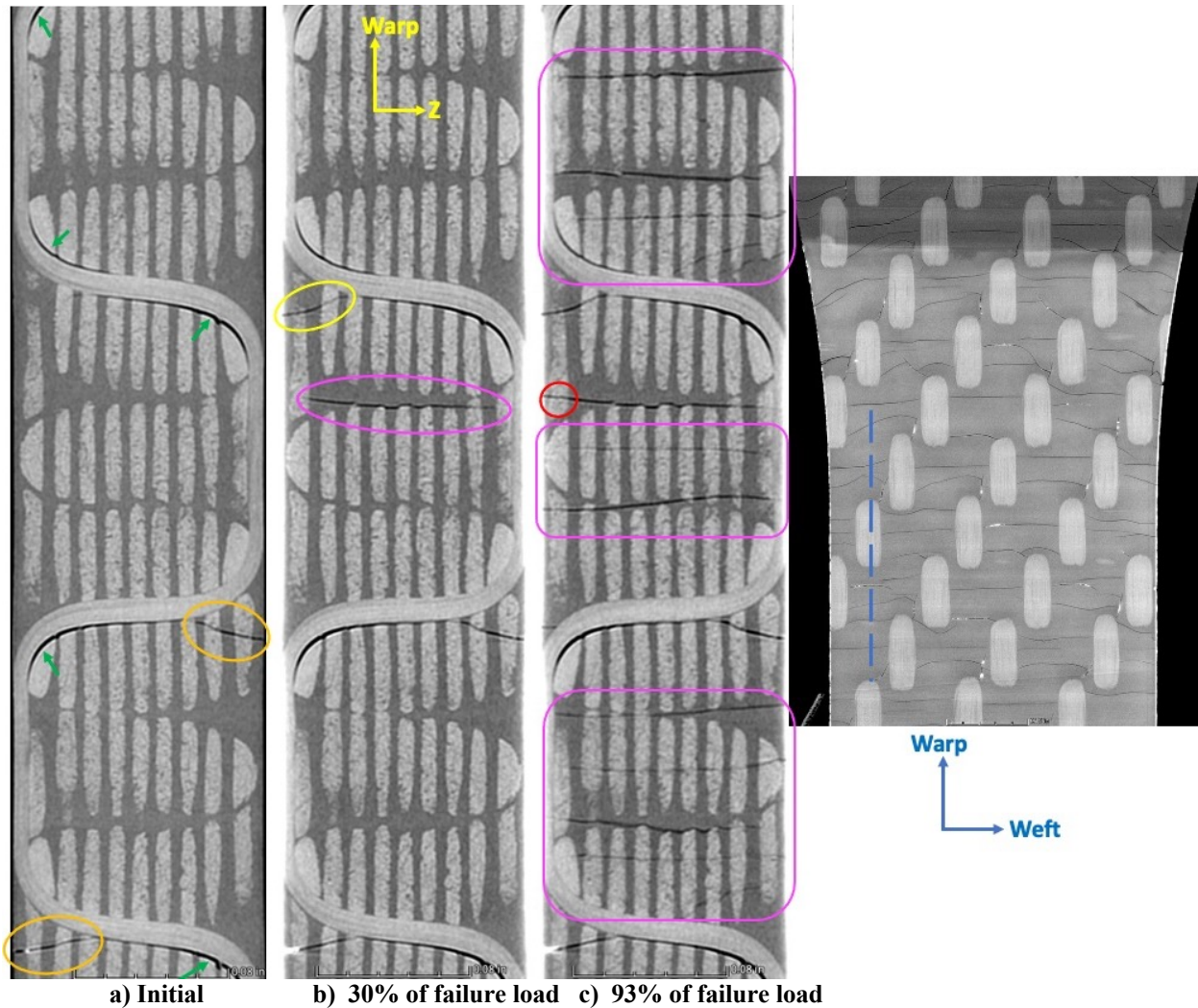American Institute of Aeronautics and Astronautics

Fig. 20 Interior cracking 1Z-TDB-M shown in X-ray CT slices between the warp tows. Surface image shows where slices were extracted. Green arrows indicate debonded Z-tows. Orange circles indicate initial cracks. Yellow and purple shapes indicate new damage.

VI. Open Hole Tension (OHT) Results

Tests were conducted on open hole tension (OHT) specimens to obtain insights into the notched failure behavior in the warp direction. Differences in the damage response between the two fabric architectures were investigated. For each panel architecture, two OHT specimens were loaded to failure and the incremental tests followed. For OHT specimens, the average failure loads (set of four specimens) were 10,673 lbs. (CV=3.3%) and 12,965 lbs. (CV=3.2%) for specimens from panels 3Z and 1Z, respectively. The structural response, failure response, surface cracking due to loading, and damage progression are detailed in this section.

A. Structural Response

The overall structural response of the OHT specimens is shown in Fig. 21, where the symbols indicate the stopping points on the incremental tests. Similar to the TDB specimens, the fracture and unloading at peak load were nearly instantaneous. The data are reported with axial stress calculated as the load divided by the unnotched cross sectional area on the ordinate and axial strain from DIC on the abscissa. To obtain the strain response, a DIC virtual extensometer with a 1.5 inch gage length was placed at the center of the specimen. In general, the initial response up to about 0.3% axial strain is linear with good repeatability. However, at higher loads, nonlinearity occurs before an abrupt failure at peak load. If the extensometer is positioned near the edge of the specimen, the response is linear up to failure. Therefore, it appears there is significant strain redistribution across the width of the specimen as it is loaded.

The average stiffness, nominal average strength, and average strain-to-failure are summarized in Table 4. The initial stiffness is obtained from this stress-strain data via a linear fit over the range 0.05% to 0.20%. The strain-to-failures reported are the center virtual extensometer strain at the last frame before the abrupt load drop at failure.
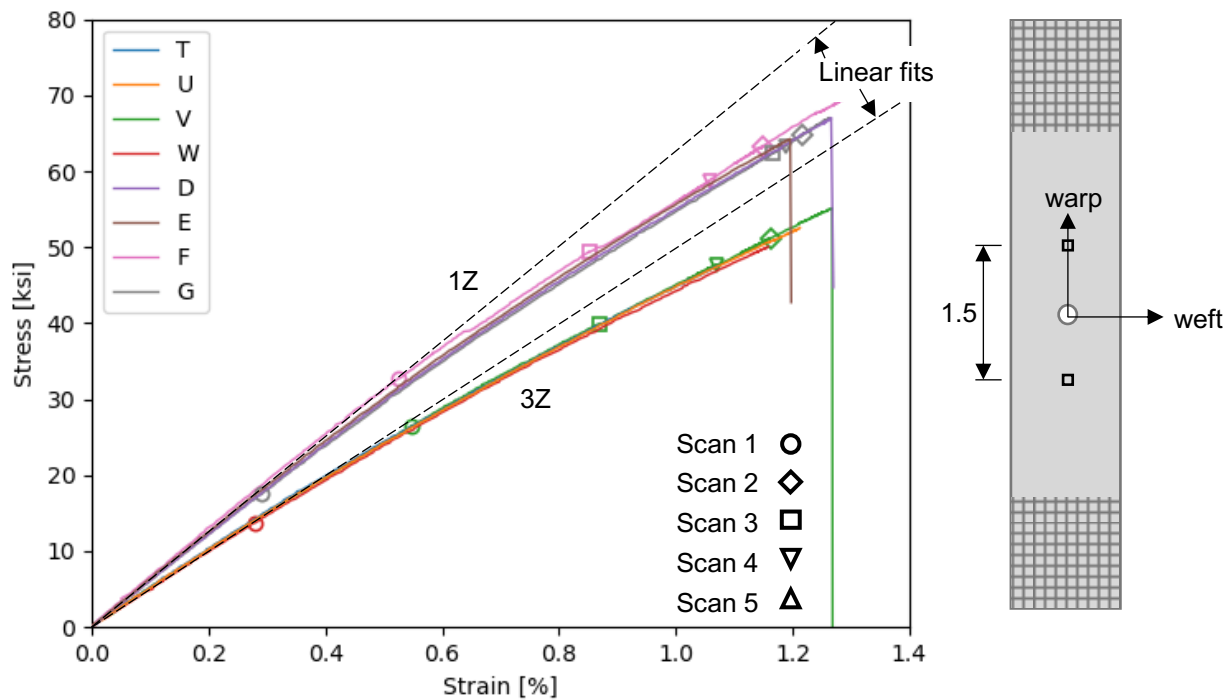

Fig. 21 Axial stress vs. strain from DIC measurement over a 1.5-inch gage length. The DIC data are extracted averaging over 0.001 in² regions.

Table 4 OHT stiffness and strength for the two weaves (panels).

Panel	Stiffness		Nominal Strength		Strain-to-failure	
	Avg. [ksi]	CoV [%]	Avg. [ksi]	CoV [%]	Avg. [%]	CoV [%]
3Z	6081	0.9	53.3	3.4	1.17	6.8
1Z	7780	1.2	67.3	3.1	1.26	3.4

B. Failure Response

Photographs of all the failed OHT specimens are shown in Fig. 22. In all cases, the through-thickness fracture propagates through the hole and normal to the loading direction. The fractures on either side of the hole are straight but are offset slightly in the axial (warp) direction. Specimens from panel 3Z had greater left-to-right offsets than specimens from panel 1Z. In general, the failure characteristics of the OHT specimens appear similar to the TDB specimens. The fracture surfaces show that the failure plane traverses across the width (weft direction) along a row of Z-tows.
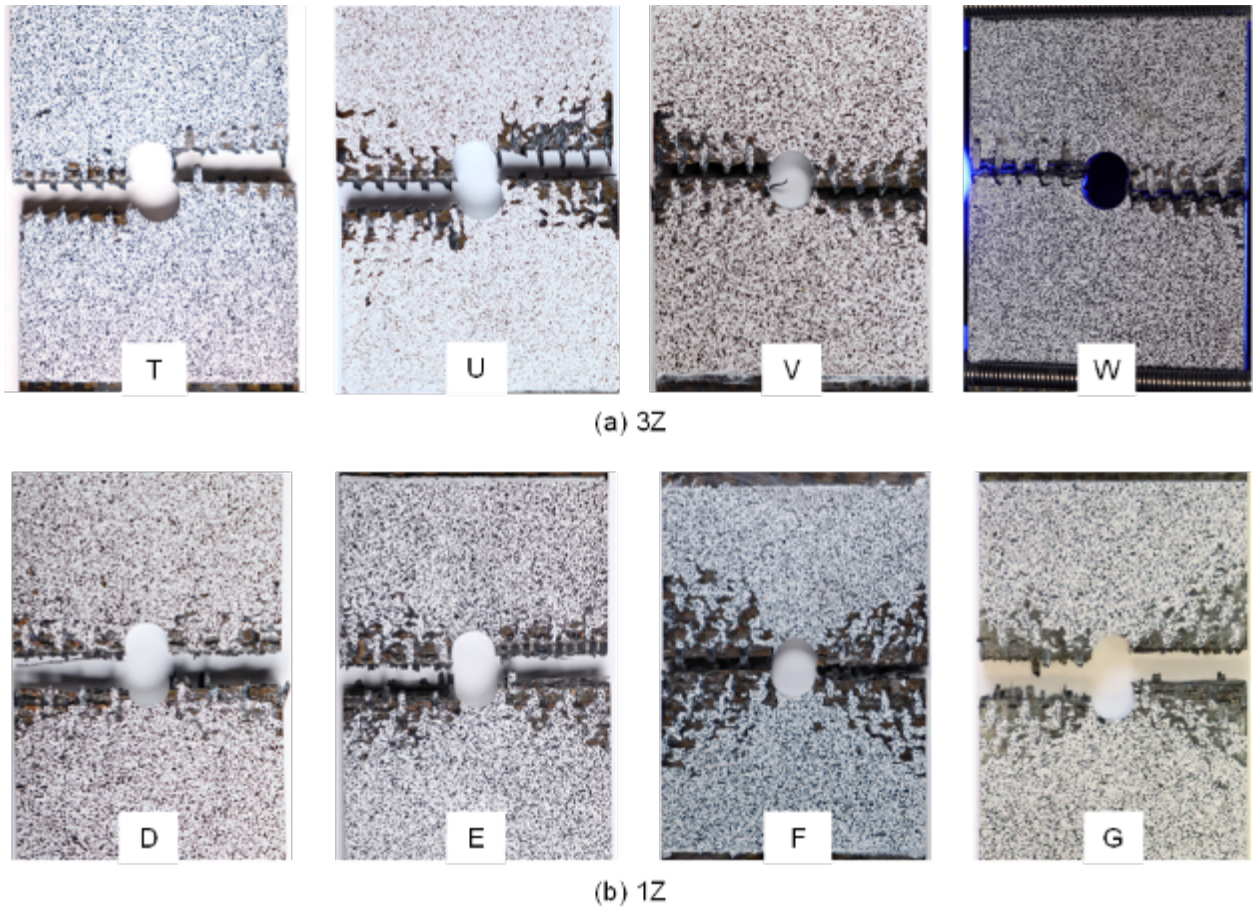
Fig. 22 Post-failure photographs of the eight OHT specimens

After failure, some of the specimens were inspected using X-ray CT. Secondary damage, not directly related to the tensile loading, was expected due to the dynamic release of energy at failure, but the primary failure region appeared to be mostly preserved. X-ray CT images of failed specimen 3Z-OHT-V are shown in Fig. 23. The planar section shown is near mid thickness, and the positions of the Z-tows are circled. The fracture path clearly follows a row of Z-tows on each side of the hole. On either side of the hole along the fracture path, through-thickness Z-tows are located at or very close to the hole edge and appear to serve as initiation sites for the fracture. The cross sections shown on either side of the hole show failures along the warp tows and in the gaps between the warp tows (at the Z-tows). The fracture path along the Z-tows also coincides with the gaps between two through-thickness stacks of weft tows. Fiber pullout of some warp tows is shown in the cross sections which is a result of tensile fractures away from the primary fracture. The fracture paths on either side of the hole are offset in the warp direction by two weft tow stacks which coincides with two Z-tow rows.
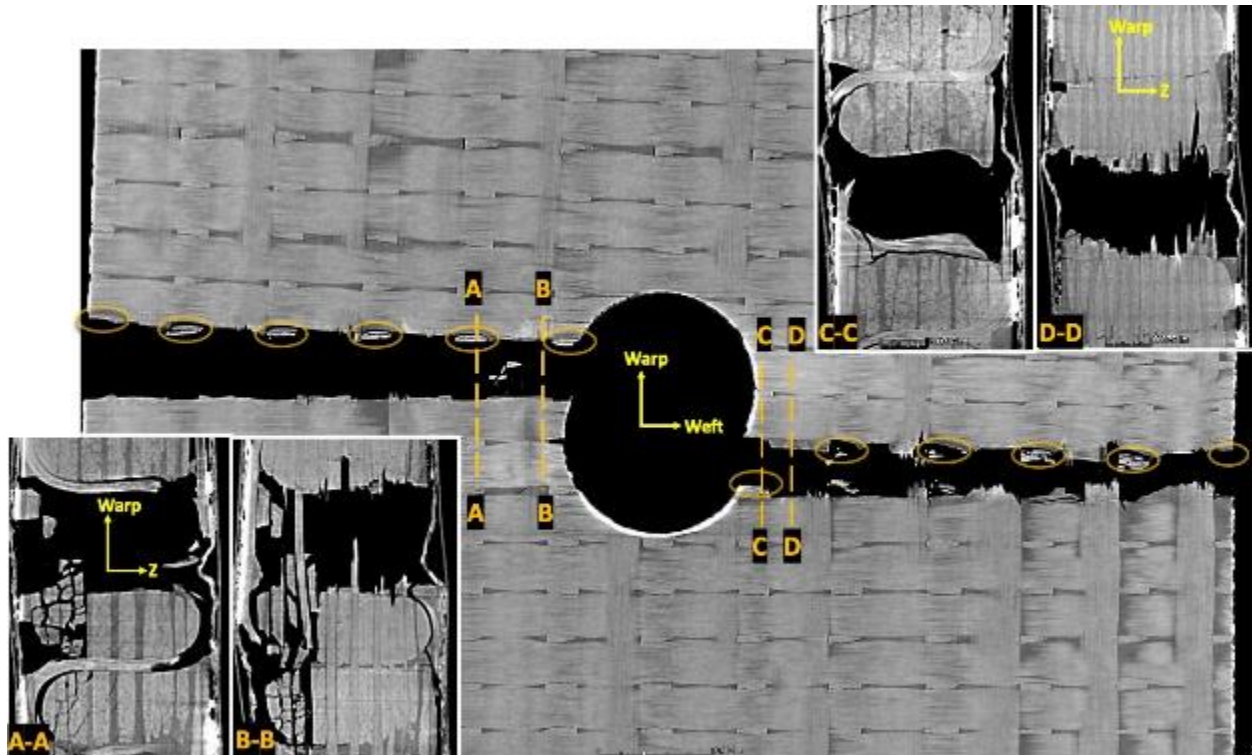
American Institute of Aeronautics and Astronautics

Fig. 23 X-ray CT failure images of 3Z-OHT-V. The locations of the Z-tows along the fracture are circled.

Specimen 1Z-OHT-G (Fig. 24) showed a similar failure to 3Z-OHT-V. Again, the fracture on either side of the hole followed a straight path across the width intersecting the through-thickness portions of the Z-tows (positions circled on the figure). On this specimen, three Z-tows happen to be located on the machined edges of the hole. Two of these edge Z-tow locations coincide with the fracture path and appear to be fracture initiation sites. The fractures are offset by one weft tow on either side of the hole. On the left side fracture near the hole, the fracture path split the weft tows (marked by arrows). One of the differences between the two fabric architectures is that, for a given axial position, the 1Z specimens have through-thickness Z-tows located after every third weft tow, and the 3Z specimens have Z-tows between every weft tow. Consequently, the fracture path between the transverse Z-tows is longer, which may contribute to a slightly more wandering crack path.
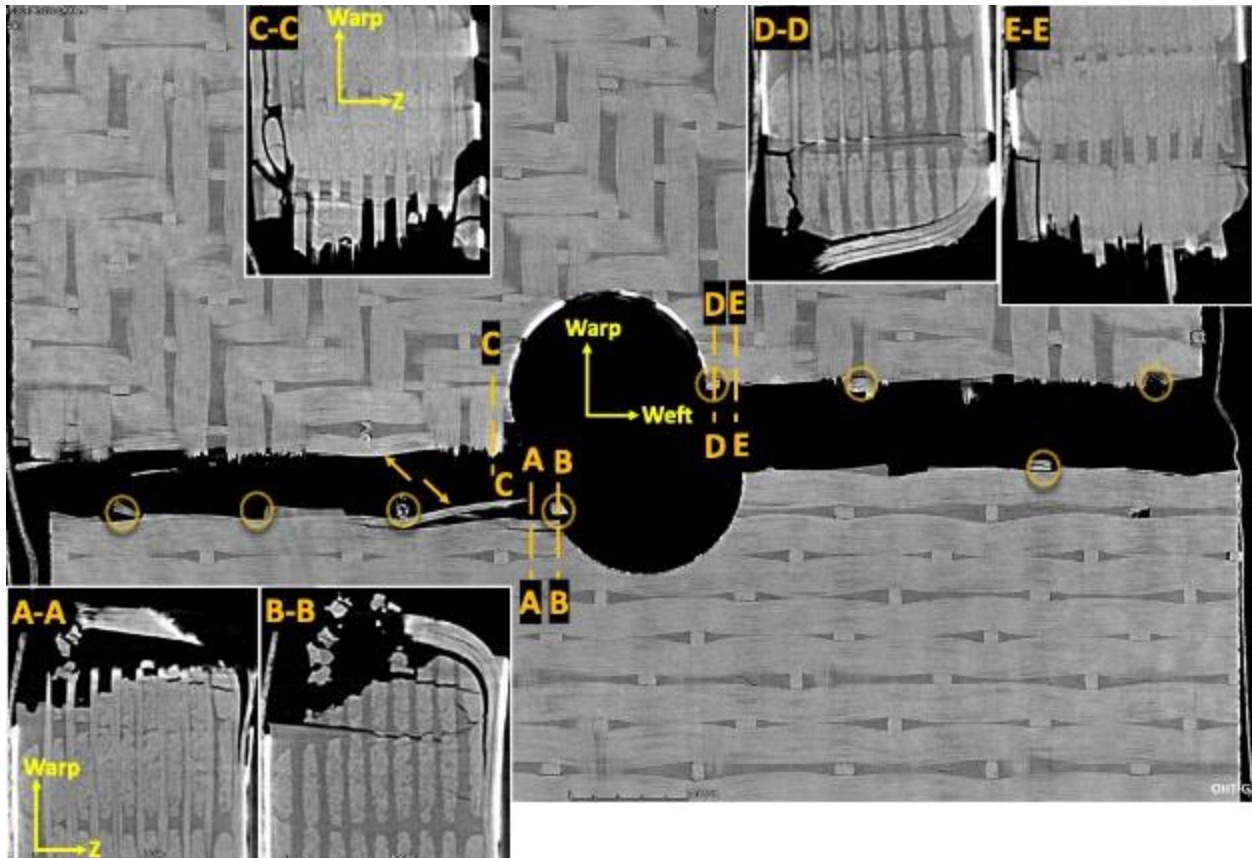
American Institute of Aeronautics and Astronautics

Fig. 24 X-ray CT failure images of 1Z-OHT-G. The locations of the Z-tows along the fracture are circled.

Failure images from the CT scan of specimen 1Z-OHT-F are shown in Fig. 25. On this specimen, the through-thickness portions of the Z-tows were not located at the hole edges. However, a similar failure to specimen 1Z-OHT-G occurred between the stacks of weft tows. Again, the fracture paths on either side of the hole were offset by one weft tow in the warp direction. The cross sections show the location of the fracture relative to the woven architecture. As shown in cross sections at the hole edge (B-B, C-C, H-H, and I-I), warp tows are partially cut by the machined edge of the hole and fracture during loading. This damage process is examined in more detail in the following section. The other cross sections show the fracture at the Z-tow and between the stacks of weft tows. An example of fiber pullout is shown in Fig. 26 for specimen 1Z-OHT-F. The planar section shown is near the mid-thickness. Sections A-A and C-C show the locations of fiber (partial tows) pullout and the fibers that have pulled out on multiple layers. The location of the fracture of these tows was traced to an adjacent crack located in the gap between warp tows and between stacks of weft tows (section B-B).

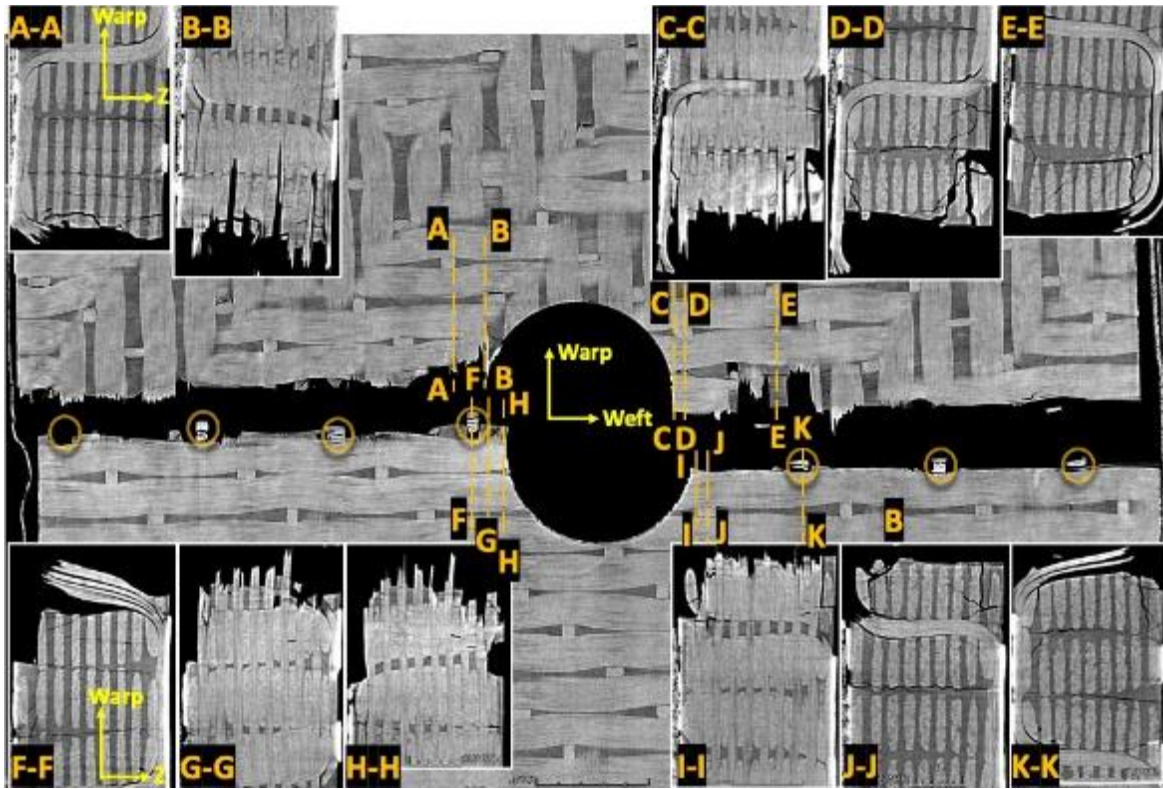American Institute of Aeronautics and Astronautics

Fig. 25 X-ray CT failure images of 1Z-OHT-F. The locations of the Z-tows along the fracture are circled.
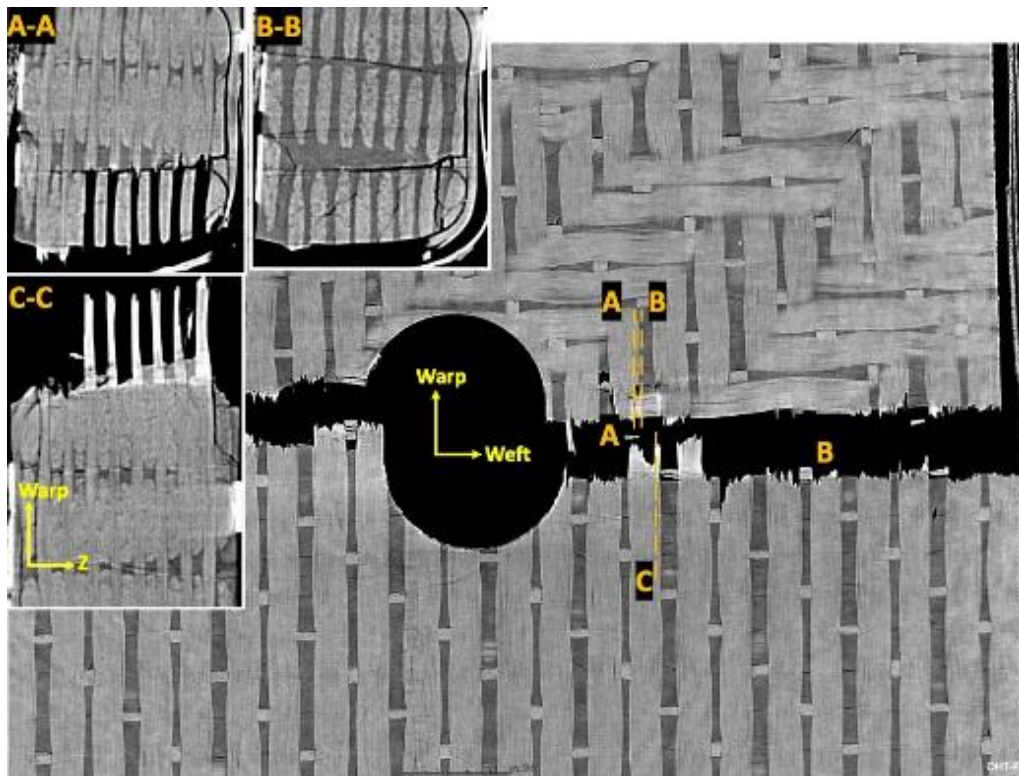

Fig. 26 X-ray CT failure images of 1Z-OHT-F highlighting fracture warp tows that have pulled out.

26

C. Surface Cracking

The DIC uncertainty coefficient sigma was used again to highlight crack formation for the OHT specimens. Contour plots of sigma at five load levels from specimens U (3Z) and E (1Z) are shown in Fig. 27. The accumulation of cracks (red regions) occurs throughout the load history starting between 20% and 40% of peak load and reaching saturation around 90% of peak load. A slight concentration of cracking near the left and right sides of the holes is noticed, but generally the cracking is diffuse. The areas above and below the hole are clearly unloaded in that no cracking is observed in these regions. On the X-ray CT images of the OHT specimens, the surface cracking away from the hole was identical to the TDB specimens for both weave architectures.

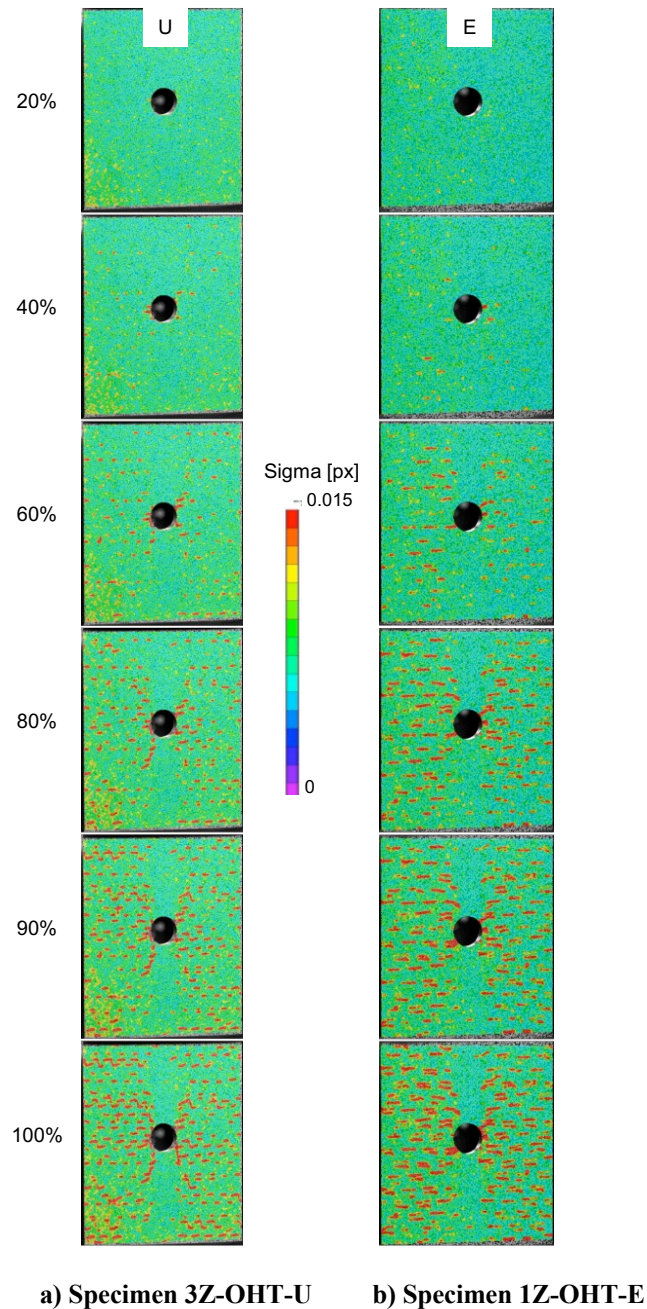a) Specimen 3Z-OHT-U   b) Specimen 1Z-OHT-E

Fig. 27 Comparison of DIC uncertainty coefficient contour plots for OHT specimens from a) 3Z and b) 1Z panels. Loading direction is vertical.

American Institute of Aeronautics and Astronautics

D. Internal Damage

The first interrupted tests from each panel (F and V) were tested to load levels identified based on acoustic emission and DIC data from the monotonic tests: 50%, 75%, 90%, 95%, of the average monotonic failure strength. In the following replicates (G and W), the first stop was at about 25% to capture the damage state at the first indications of damage and then subsequent stops attempted to capture the damage state as close as possible to the maximum load. The interrupted loading run load levels are summarized in Table 5 and are shown with symbols in Fig. 22. Specimen W failed at a relatively low stress, and so only two loading runs were conducted. In the final loading, the specimens were loaded to failure, with F_{max} being the maximum recorded load.

Table 5 OHT interrupted test load levels.

Panel	Specimen	Run	Fraction of strength [%]	Fraction of average strength [%]
3Z	V	1	48.0	49.7
		2	72.6	75.0
		3	86.5	89.5
		4	92.9	96.0
		5	100.0	103.4
	W	1	27.0	25.7
		2	100.0	95.2
1Z	F	1	45.1	47.1
		2	70.5	73.7
		3	83.7	87.5
		4	90.3	94.3
		5	100.0	104.5
	G	1	26.3	26.3
		2	93.1	93.1
		3	94.5	94.5
		4	96.8	96.8
		5	100.0	100.0

The progressive damage in specimen 3Z-OHT-V was documented by conducting X-ray CT scans during the stops in loading at 48%, 73%, 87%, 93% of F_{max}, and after failure. In Fig. 28, a comparison between the initial scan and a scan after loading to 93% of F_{max} is shown for a mid-thickness section around the hole. The failure path, which follows the Z-tows, is marked on the second scan to highlight indications of possible failure initiation sites. Damage caused by the tensile load is indicated by yellow arrows. Four Z-tows are shown along the fracture path. On the left side crack path, the outer Z-tow appears to debond while the Z-tow at the hole had an initial crack that does not appear to grow under loading. On the right side, the outer Z-tow shows initial cracking with additional crack growth toward the hole. The Z-tow at the hole had an initial crack that extended to the hole, and a debond formed on the top of the tow. Other notable damage, not on the fracture path, included a debonded and displaced Z-tow (9:00 position) and weft-direction cracks forming at the 10:00 and 2:00 positions.

For the same specimen, damage progression is shown in through-thickness cross sections for the left and right sides of the hole in Figs. 29 and Fig. 30, respectively. The failure location is highlighted across the sections, and new damage growth between runs is circled. For the left side of the hole (Fig. 29), the image after 48% of F_{max} shows cracks (circled in yellow) branching off from the through-thickness portion of the Z-tow and connecting to the surface (or near to it), similar to the behavior observed in the TDB specimens. After 73% of F_{max}, more of these types of cracks develop, and the Z-tow at the 9:00 o'clock position is debonded (red box). After 87% of F_{max}, matrix cracks develop that do not connect to the surface and typically remain within a stack of weft tows (circled in green). Between 87% and 93% of F_{max}, the damage state remains almost the same with the exception of one new crack that spans to the surface from the Z-tow (circled in yellow). A similar damage progression is shown for the right side of the hole (Fig. 30). However, after 87% of F_{max}, a new crack (orange circle) forms above the Z-tow where the fracture will occur. The post-failure images on both figures show the failure at the Z-tow as well as some additional damage due to the large energy release. In general, the damage looks very similar to the TDB specimens with some limited damage developing along the eventual fracture path prior to failure.

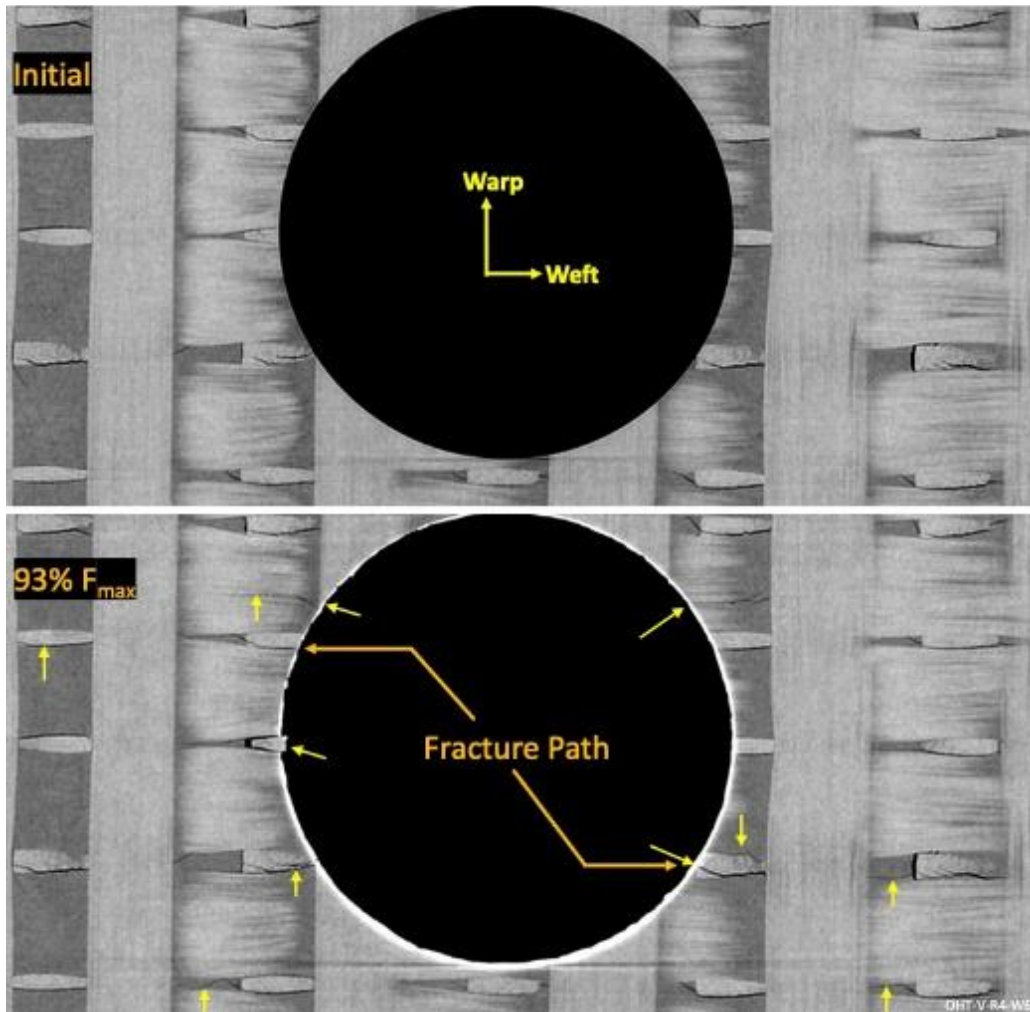American Institute of Aeronautics and Astronautics

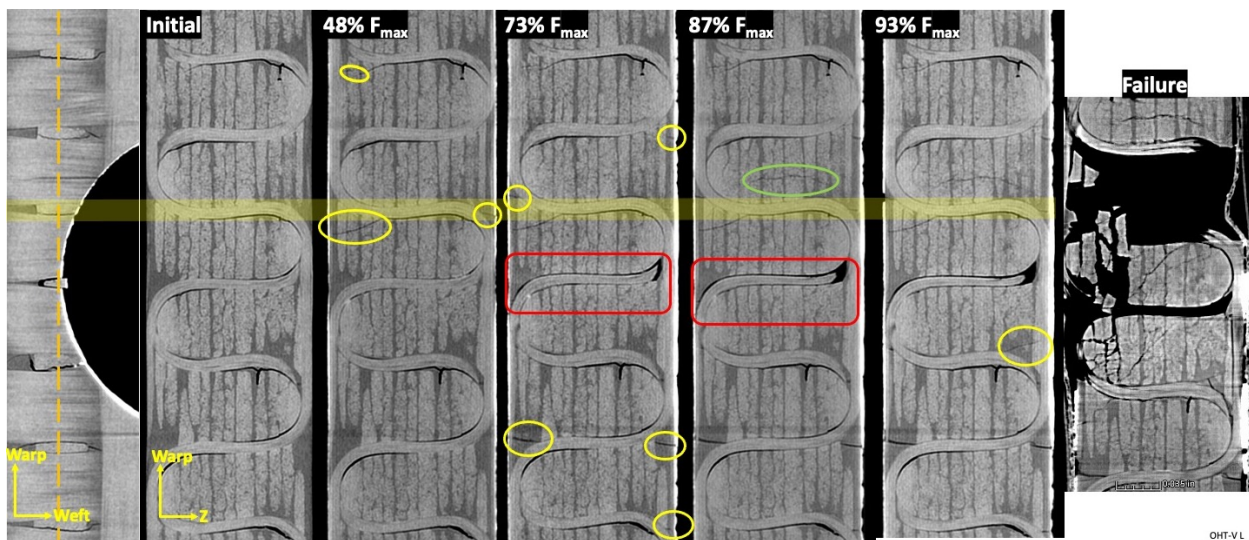**Fig. 28 X-ray CT failure images of 3Z-OHT-V. Damage from loading is marked with arrows.**

Fig. 29   X-ray CT progressive damage images near the left side of the hole for specimen 3Z-OHT-V. The locations of damage growth are circled.

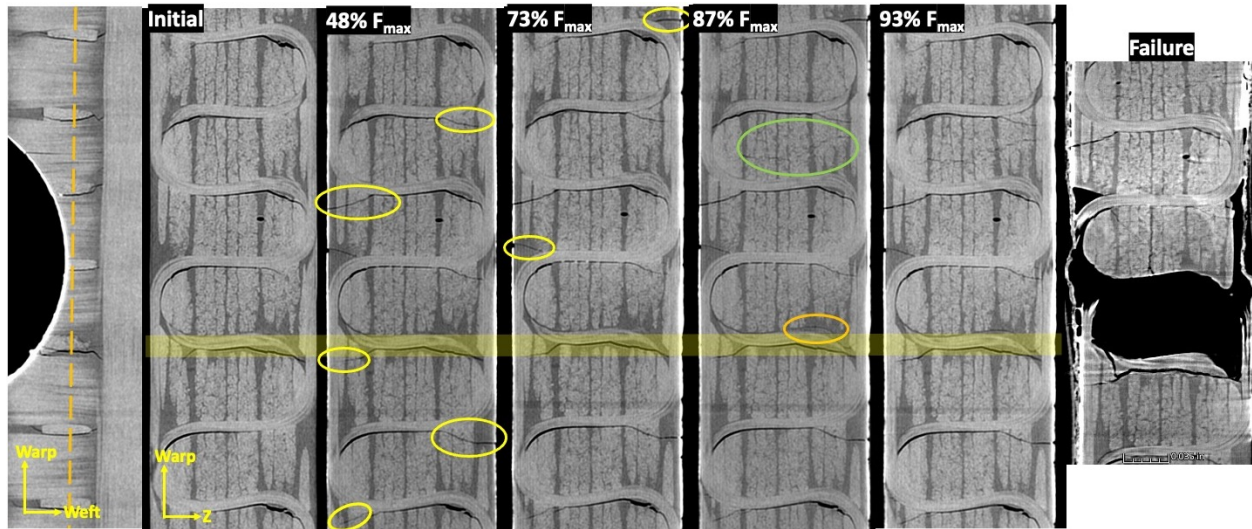American Institute of Aeronautics and Astronautics

Fig. 30   X-ray CT progressive damage images near the right side of the hole of 3Z-OHT-V. The locations of damage growth are circled.

For panel 1Z, damage development near the hole is shown in Fig. 31 on adjacent slices through the weft and warp tows near the mid-thickness for specimen OHT-F after loading to 90% of F_{max}. This specimen does not have Z-tows at the hole edge, but the machining of the hole has removed a small section of warp tow fibers on the left side and most of the warp tow fibers on the right side (Fig. 31b). Pre-test images show that the initial damage is primarily debonding of the Z-tows with branching cracks curving between the warp tow layers (orange circles). Two additional cracks were also found between the warp tows away from the Z-tows (green circles). The lower crack intersects the hole edge and can also be seen intersecting the weft plane (green circle). The damage resulting from loading to 90% of F_{max} is circled on the lower images. On the warp tow plane (Fig. 31b), many cracks, normal to the warp direction, are shown developing in the gaps between the warp tows on both sides of the hole (circled). On the left side, the slice through the layer of weft tows shows the development of two cracks between the weft tows that connect to the hole edge (purple circles). One of these cracks, corresponding to the eventual fracture path, connects to the initial Z-tow crack and continues away from the hole (blue circle). A new crack in the warp direction also appears in the resin pocket near this Z-tow with a corresponding split between the fibers in the adjacent warp tow (blue arrows). On the right side, three cracks, located between the weft tows, are observed connecting to the hole edge (purple circles). These three cracks are also visible on the warp layer and are marked with red and purple circles. The middle crack (circled in red) connects to the broken fibers along the warp tow that was cut by the hole and corresponds to the fracture path.

Damage progression of the warp tow fracture is shown in a series of through-thickness slices in the warp direction adjacent to the hole in Figs. 32-33 for specimen OHT-F. Damage progression is shown in Fig. 32 from the initial state to images taken after 47%, 71%, 84% of F_{max}, and post-failure for a cross section in the warp tow gap adjacent to the failed tow. The initial damage state shows debonding of the Z-tows (orange arrows) and some cracks connecting to the surface (orange circles). After 47% of F_{max}, through-thickness cracks have formed between the stacks of weft tows near the hole (green circles). Additional cracks branch off from the interior Z-tows and toward the surface (yellow circles). After 71% of F_{max}, more cracks form between the weft tow stacks just above and below the hole (green circles). Small cracks also form within the weft tow stacks (purple circles). After 84% of F_{max}, more small cracks appear within the weft tow stacks (purple circles). Testing for specimen OHT-F was also stopped at 90% of F_{max}, but no new cracks or damage growth was detected. The final cross section shows the failure between stacks of weft tows corresponding to a crack first observed after 47% of F_{max}.

A similar progression of X-ray CT cross sections is shown in Fig. 33 along the warp tow that developed fiber fractures. After 47% of F_{max}, a through-thickness series of small cracks appear between the warp tows as marked by arrows. These cracks follow the two crack paths between the weft tow stacks nearest to the hole that are shown in Fig. 32. After 71% of F_{max}, six of the eight warp tows along the lower series of cracks show fiber fractures. After 84% of F_{max}, the remaining two warp tows have fiber fractures along this series of cracks. At failure, the specimen separates along this line of warp tow fractures.

a) Weft plane near mid thickness   b) Warp plane near mid thickness

Fig. 31 X-ray CT images showing damage development in adjacent a) weft and b) warp planes for specimen 1Z-OHT-F. Damage locations are circled.

Fig. 32 Through-thickness X-ray CT sections in the warp tow gap showing damage progression for specimen 3Z-OHT-F. The locations of additional damage from the previous run are circled.
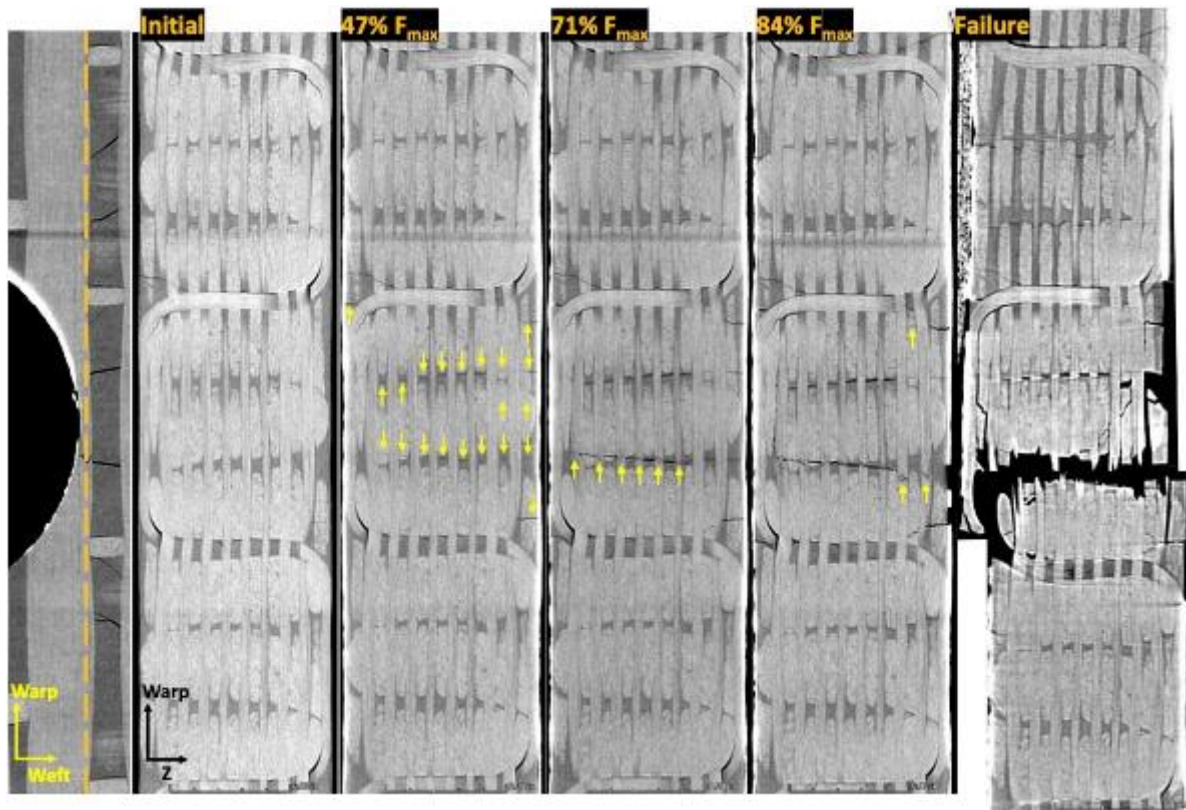
31

Fig. 33 Through-thickness X-ray CT sections in the warp tow showing damage progression for specimen 1Z-OHT-F. The locations of additional damage from the previous run are indicated by arrows.

The progressive fracture is shown in Fig. 34 for the other 1Z specimen (OHT-G) where the outer edge of the hole intersects the interior portion of a Z-tow instead of a warp tow. In the gap between the warp tows, cracks develop near the hole. After 26% of F_{max}, a new crack is shown near the hole-edge Z-tow that connects the Z-tow debonding to the surface (yellow circle). By 93% of F_{max}, extensive cracking has developed near the hole edge. Through-thickness cracks are observed between and within the weft tow stacks (green circles). Additonal crack formation (green circle) is shown within a weft tow stack in the section after loading to 94% of F_{max}. It is also interesting to note that two small cracks have formed near the large void at the bottom of the cross-section images (blue circles). Specimen fracture occurs at the hole-edge Z-tow and continues between the weft tow stacks to the specimen edge. Thus, despite having a different condition in terms of the location of the hole relative to the weave pattern, OHT-G and OHT-V show similar matrix cracking patterns, and final failure locations with respect to the weave pattern.

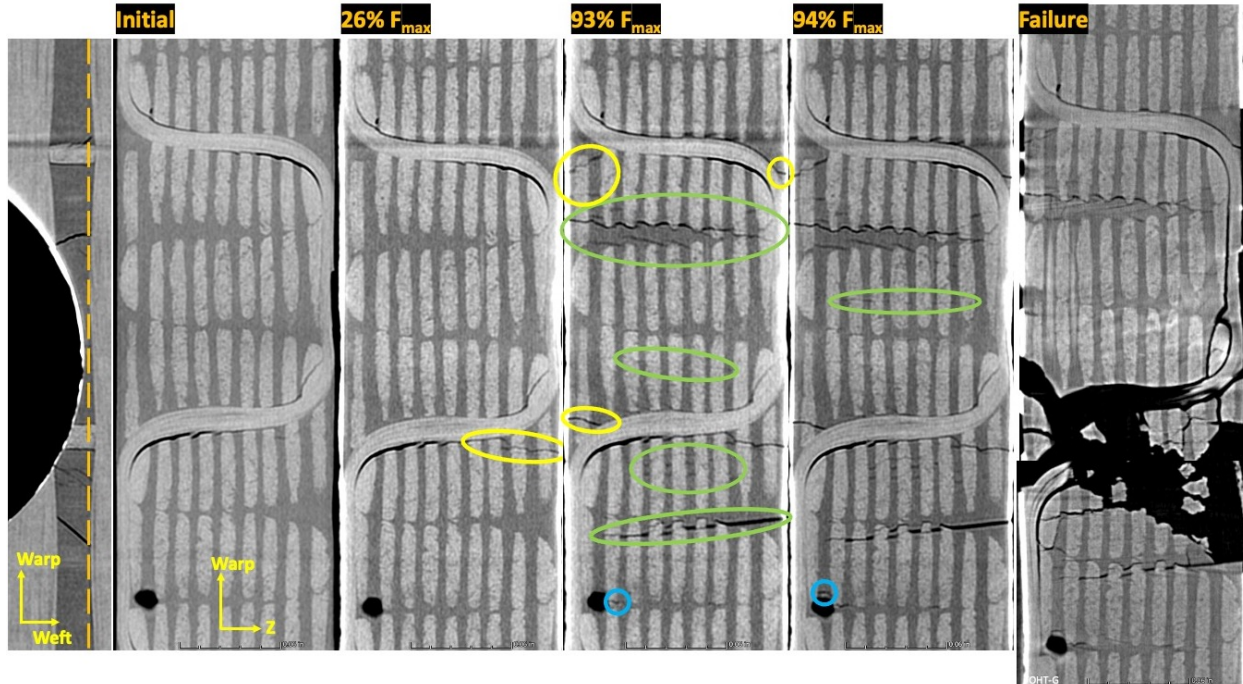American Institute of Aeronautics and Astronautics

Fig. 34 Through-thickness X-ray CT sections in the warp tow gap showing damage progression for specimen 1Z-OHT-G. The locations of additional damage from the previous run are circled.

VII. Summary and Concluding Remarks

The damage mechanisms in 3D orthogonal woven specimens were investigated using unnotched (dogbone) and notched (open hole) tensile coupons loaded in the warp direction. Tests were performed on specimens with two different weave patterns. Weave 3Z has 13 layers of weft tows, 12 layers of warp tows, and three Z-tows per dent. Weave 1Z has 9 layers of weft tows, 8 layers of warp tows, and one Z-tow per dent. The most significant difference between the two architectures is that 3Z has a through-thickness tow between every weft tow, while 1Z has a through-thickness tow after every third weft tow. Each test series consisted of monotonically loading two specimens straight to failure and incrementally loading two specimens to failure. Digital Image Correlation (DIC) was used to obtain the overall structural response and the surface response. X-Ray CT scanning was used to obtain the initial and incremental damage states during interrupted tests and was used to document the fracture paths and mechanisms of some specimens after failure.

Pre-test X-ray CT inspection revealed a significant amount of matrix cracking due to manufacturing in all specimens. Most of the interior cracking was related to the through-thickness Z-tows. Nearly all Z-tows were partially debonded. There were many instances of cracks branching from the Z-tow debonding towards the surface while passing between the fibers of the weft tows. In addition, cracks also propagated from the Z-tow debonding into the resin rich pockets between or in the warp tow layers. Numerous surface cracks and voids were also found.

The dogbone specimens had a linear response up to an instantaneous failure event that resulted in two-piece failure. DIC was used to create maps and accumulation plots of the surface cracking as a function of load. Surface cracking started at 20-30% of peak load and reached saturation around 90% of peak load for all specimens. All failures were straight across the width of the specimen (in the weft direction) with a fracture path that followed a row of Z-tows. Since the 1Z specimens only had a Z-tow after every third warp tow along the fracture path, the path wandered slightly between the Z-tows. The final failure location was in the transition region where a stress concentration exists since the specimen width is reduced from 1.0 in. to 0.6 in. In this transition region, stacks of warp tows are terminated on the curved edges. When the warp tow stacks end near an edge Z-tow, an even larger stress concentration is created which likely causes failure. All failures that were investigated were traced to a cut warp tow stack located near an edge Z-tow in the transition region. These locations likely experience a particularly high stress concentration since both the specimen geometry and weave architecture contribute. The incremental testing showed accumulation and propagation of matrix cracking, primarily in the gaps between the warp tow stacks, with increasing load. Internal cracking was observed by 30% of F_{max} in both weaves. However, new cracks and crack growth appeared to stop after

33

90% of F_{max}. The cracks were primarily normal to the loading direction. In the 1Z specimens, through-thickness cracks first developed between stacks of weft tows then within the weft stacks at higher loads. In the 3Z specimens, through-thickness cracks only occurred as branches from debonded Z-tows and were not observed just within the stacks of weft tows. Despite achieving high fractions of the final peak load, no evidence of fiber fracture in the tows was found in the X-ray CT scans.

A similar investigation was performed on the open-hole specimens. The mechanical response of each specimen was assessed using a DIC virtual extensometer with a 1.5 inch gage length placed at the center of the specimen. The initial response up to about 0.3% axial strain is linear with good repeatability. At higher loads, some nonlinearity is observed. An abrupt two-piece failure occurred at peak load. The nonlinearity may be caused by load redistribution as a result of damage formation around the hole. Similar to the TDB specimens, all fracture paths followed rows of Z-tows. However, the fracture paths were offset in the axial direction on either side of the hole. Z-tows that were located on the hole perimeter were the most likely location for a specimen fracture. Cracking near the hole primarily developed in the resin-rich regions between the weft tows and was found in specimens loaded to less than 30% of F_{max}. The positioning of the hole relative to weave geometry was random, and therefore provides some additional insight into the interaction of different aspects of the weave with the stress concentration. When the hole placement was such that it removed a portion of a warp tow (as opposed to removing complete tows), fiber fracture was observed in the reduced section of the warp tow before final failure, and the final fracture path connected through this fractured tow. The location of this warp tow fracture is connected to cracking in the resin rich regions between the weft tow stacks. Apparently, the load was seamlessly redistributed to the remaining warp tows, since no evidence of fiber failure in the partial warp tows was found in the structural response or DIC data.

The notched and unnotched failures for these 3D woven materials appear very similar in terms of damage mechanisms, damage propagation, and post-failure fracture paths. The following behaviors were common to both weave patterns and both test specimens.
1. The primary region of matrix cracking is in the resin-rich region between the warp tows, and these cracks tend to follow paths between the weft tows. In general, the crack surface normals are in the load direction, although some curved cracks were observed around the Z-tows. No cracks resembling delamination were observed prior to peak load.
2. Matrix cracking starts at relatively low loads (<30% of F_{max}) and continues to increase until approximately 90% of F_{max}. Surface cracking is extensive, but most surface cracks stop at the outer most layer of warp tows. In general, matrix cracks propagate until they reach fibers oriented across the crack surface, at which point the crack propagation arrests.
3. The manufacturing induced cracking around the Z-tows linked up with matrix cracks that occurred due to loading, and therefore alternative processing that reduces or eliminates this cracking may increase the strength.
4. Final failure occurs abruptly when fiber failure occurs. In OHT specimens, where the hole machining resulted in partially removed warp tows, fiber failure was observed locally prior to reaching the maximum load, but there was no observable impact of this fiber failure on the structural response. In all other cases, fiber failure was not observed prior to reaching the max load.
5. There is evidence that the failure location is determined by interaction between the weave geometry and the specimen geometry. Fractures always followed a row of Z-tows located near stress concentrations resulting from the specimen geometry.

Acknowledgments

References

[1] M. N. Saleh and C. Soutis, "Recent advancements in mechanical characterisation of 3D woven composites," *Mechanics of Advanced Materials and Modern Processes,* pp. 1-17, 2017.

[2] M. Ansar, X. Wang and C. Zhou, "Modeling strategies of 3D woven composites: A review," *Composite Structures,* pp. 1947-1963, 2011.

[3] S. D. Green, M. Y. Matveev, A. C. Long, D. Ivanov and S. R. Hallett, "Mechanical modelling of 3D woven composites considering realistic unit cell geometry," *Composite Structures,* vol. 118, pp. 284-293, 2014.

American Institute of Aeronautics and Astronautics

[4]   D. P. Patel, A. M. Waas and C.-F. Yen, "Direct numerical simulation of 3D woven textile composites subjected to tensile loading: An experimentally validated multiscale approach," *Composites Part B: Engineering,* vol. 152, pp. 102-115, 2018.

[5]   Y. Chai, Y. Wang, Z. Yousaf, N. T. Vo, T. Lowe, P. Potluri and P. J. Withers, "Damage evolution in braided composite tubes under torsion studied by in-situ X-ray computed tomography," *Composites Science and Technology,* vol. 188, p. 107976, 2020.

[6]   D. Mollenahuer, E. Becker, L. Ferguson, E. Iarve, K. Hoos, H. K. Adluru, E. Zhou, D. Riha, M. Stanfield, A. Selvarathinam and S. Engelstad, "Process-to-Performance Simulation of 3D Woven Composite T-Joints," in *AIAA Scitech 2021 Forum*, Virtual, 2021.

[7]   T. Ricks, E. Pineda, B. Bednarcyk and S. Arnold, "Progressive Failure Analysis of 3D Woven Composites via Multiscale Recursive Micromechanics," in *SciTech 2021*, Virtual, 2021.

[8]   A. Bergan, "An Automated Meshing Framework for Progressive Damage Analysis of Fabrics Using CompDam," in *American Society for Composites 35th Technical Conference*, Virtual, September 14-17, 2020.

[9]   K. C. Warren, A. L.-A. Roberto and J. Goering, "Experimental investigation of three-dimensional woven composites," *Composites Part A: Applied Science and Manufacturing,* vol. 73, pp. 242-259, 2015.

[10]   A. E. Bogdanovich, M. Karahan, S. V. Lomov and I. Verpoest, "Quasi-static tensile behavior and damage of carbon/epoxy composite reinforced with 3D non-crimp orthogonal woven fabric," *Mechanics of Materials,* vol. 62, pp. 14-31, 2013.

[11]   M. Pankow, B. Justusson, M. Riosbaas, A. M. Waas and C. F. Yen, "Effect of fiber architecture on tensile fracture of 3D woven textile composites," *Composite Structures,* vol. 225, p. 111139, 2019.

[12]   N. Castaneda, B. Wisner, J. Cuadra, S. Amini and A. Kontsos, "Investigation of the Z-binder role in progressive damage of 3D woven composites," *Composites Part A: Applied Science and Manufacturing,* vol. 98, pp. 76-89, 2017.

[13]   R. Muñoz, V. Martínez, F. Sket, C. González and J. Llorca, "Mechanical behavior and failure micromechanisms of hybrid 3D woven composites in tension," *Composites Part A: Applied Science and Manufacturing,* vol. 59, pp. 93-104, 2014.

[14]   "ASTM Standard D5766. Standard Test Method for Open-Hole Tensile Strength of Polymer Matrix Composite Laminates," in *Annual Book of ASTM Standards*, ASTM Int., 2018.

[15]   Correlated Solutions Inc., *VIC-3D, Software package, 2010.1.0.*

[16]   Mathworks, "Color-Based Segmentation Using the L*a*b* Color Space," 2021. [Online]. Available: https://www.mathworks.com/help/images/color-based-segmentation-using-the-l-a-b-color-space.html.

American Institute of Aeronautics and Astronautics